The Dissertation Committee for Xubing Zhou certifies that this is the approved version of the following dissertation:

Photoemission Study of Stepped surface, Thin Film and Nanowire Growth

Committee:

James L. Erskine, Supervisor

John Markert

Zhen Yao

Maxim Tsoi

Alan Campion

Photoemission Study of Stepped Surface, Thin Film and Nanowire Growth

by

Xubing Zhou, B.S.; M.S.

Dissertation

Presented to the Faculty of the Graduate school of

The University of Texas at Austin

in Partial Fulfillment

of the Requirements

for the Degree of

Doctor of Philosophy

The University of Texas at Austin

December 2008

Acknowledgements

First I would like to thank my Ph.D. supervisor, James L. Erskine for his continued guidance, encouragement and support. I would also like to thank the machine shop in the UT physics department. They made a lot of delicate parts for me during the past five years. I would like to thank John Scott and other people in CAMD and LSU physics department for their help during the one year period I was in Baton Rouge. I would like to thank Shuqiang Yang, David Lacina, Jusung Yang and other people in the Lab for help. Finally I would like to thank my parents for their endless support.

Photoemission Study of Stepped surface, Thin Film and Nanowire Growth

Publication No._______________________

Xubing Zhou, Ph.D.

The University of Texas at Austin, 2008

Supervisor: James L. Erskine

Steps on a high index metal or semiconductor surface may play a fundamental role for electronic structure, adsorption, film growth, chemical reaction and catalysis. The surface atomic and electronic structures of stepped W(110) surfaces have been investigated by a few research groups during the past 20 years. But there is still a lot of controversy. We use high resolution core level photoemission to study several different stepped tungsten surfaces. Curve fittings of the spectra permit tests of core-level binding-energy shift models that relate local atomic coordination to binding -energy differences associated with terrace and step-edge atoms. For the first time we find a well resolved $W4f_{2/7}$ peak associated with step edge atoms. We attribute previous failure to directly detect the step-edge effects in core level photoemission to contamination by hydrogen. The well resolved peaks for surface atoms with different coordinations can serve as a "finger print" for specific atoms. Experiments in which stepped surfaces are systematically dosed by H_2 clarify the role played by H contamination. We also grow Ag nanowires on the stepped W(110) surface and use angle resolved photoemission to study the band structure. We find distinct dispersion for the nanowires along the step edge direction while there is only little dispersion perpendicular to the wires.

The second part of the research is core level photoemission study on Cesium film growth on Cu(100) surface. We study the phonon broadening effect for Cs at different temperatures. We compare our data with previous theoretical models and get good results on surface and bulk Debye temperatures and zero temperature phonon broadening. The binding energy shifts for the Cs $5p_{2/7}$ at different temperatures have also been investigated. The results fit the lattice expansion model very well except at temperature higher than 200 K. The higher temperature deviation is caused by thermal evaporation of Cs films. This conclusion is checked by the following coverage dependent core level peaks study on the Cs/Cu(100) system.

Table of Contents

Chapter 1

A review of atomic and electronic structures of stepped surfaces , nanowire growth and catalysis studies 1

1.1 Core level and angle resolved photoemission study on atomic and electronic structures for stepped tungsten surface 2

1.2 Stepped surface used as one dimensional defects for catalysis 8

1.3 Core level photoemission study on stepped semiconductor surface 12

1.4 Nanowires growth on metal substrates 12

Chapter 2

Photoemission theory and experimental methods 16

2.1 Ultra high vaccum 16

2.2 Electron spectroscopies 17

2.2.1. Photoemission spectroscopy 18

2.2.2 Low-energy electron diffraction (LEED) 19

2.2.3. Auger Electron Spectroscopy (AES) 22

2.3 Photoemission General Theory 24

2.4 Core level photoemission study and Doniach-Sunjic lineshapes 28

2.5 Electrostatic analyzer 32

2.6 Photoemission light sources 35

2.6.1 The discharge lamp 36

2.6.2 Synchrotron light sources 36

2.7 Sample making and ex-situ preparation 43

Chapter 3

Photoemission study on stepped tungsten W(110) surface 50

3.1 Core level photoemission study on stepped W(110) surface 50

3.2 Angle resolved photoemission study on nanowire growth on stepped W(110) 67

Chapter 4

Core level photoemission study on Cs film growth on Cu(100) 70

4.1 Phonon broadening study of Cs $5p_{3/2}$ core level spectra 71

4.2 Binding energy shifts study of Cs 5p core level spectra 82

4.3 Coverage dependence study of Cs/ Cu(100) 88

Appendix

Bibliography 92

Vita 100

Chapter 1

Introduction to photoemission study on atomic and electronic structures of stepped surfaces, adsorptions and nanowire growth

Photoemission spectroscopy (PES) has been used to investigate surface atomic and electronic structures for many years. Depending on the photon energies, PES can study both valence and core states. While the valence PES can often give you surface band structure and information around Fermi energy, the core level PES can let you know more about the chemical environment around certain types of surface atoms. During the past 10 years, technology has developed rapidly and both energy and angular resolution of the PES have been improved significantly. With the state of art Scienta analyzer extremely high energy resolution of sub-meV and angular resolution smaller than 0.1 degrees have been achieved. At the same time, a very powerful photon source, the third generation synchrotron radiation has been built on several places in the world. These technology advances offer great opportunities for surface science studies that cannot be attempted 20 years ago.

Core level photoemission has proved to be a very powerful method for surface science study. The major advantage of this method is due to its element specificity. The binding energies of core states are different from element to element. Thus the core level photoemission measurement can often determine the elemental composition on a surface.(Its surface sensitivity credits to the short mean free path of photoelectrons inside the solid) Also core level binding energy measurements in photoemission are sensitive to the chemical environment of a specific atom. Different bondings cause different core level shifts. The development of instrumentation that can measure this chemical shifts accurately enough was rewarded a Nobel Prize in 1981(the so-called “Electron Spectroscopy for Chemical Analysis” or ESCA). Not only the core level shifts can detect the chemical environment of a surface atom, but also it can measure different surroundings of the same type of element, e.g. different coordinations often give different Surface Core Level Shifts (SCLS). This type of study usually needs higher resolution than the chemical shift study due to the smaller SCLS. In addition to the measurement of small core level shifts, core level photoemission also allows you to study the dynamical process of core and valence electronic states through the core level lineshape study. In this introductory review, I will first desbribe core level line shift study of single crystal metals, especially for stepped surface. Valence band studies on the stepped surface are also introduced as a different perspective of view. Then I will give examples for adsorption and catalysis study by the core level PES. Last I will introduce the core level study on nanowires. Other type of methods for investigating nanowire growth and recent development are listed on the appendix.

1.1 Photoemission study on flat and stepped single crystal surfaces

Surface core level shift study on single crystal has been going on for several decades. Many crystals have been found to exhibit significant surface binding energy shifts from the bulk value. A good example is W(110) surface. The SCLS has a large value of about 320 meV. You can easily detect the difference between the top layer tungsten atoms and atoms under the top layer. However, there has been no observation till now that the second layer can be distinguished from the bulk due to the very small core level shift. We know that the coordination of the second layer atoms should be different from the bulk due to different numbers of second nearest neighbors. Even the third and fourth layer atoms are ensentially different from the bulk. This reasoning justifies the constant development of analyzer and synchrotron radiation to achieve better resolution. Only not long ago, it was found that surface related core level shifts of Be(0001) extends far below the top layer and even the fourth layer 1s binding energy can be distinguished from the bulk.[64] Fig 1.1 shows the core level spectrum for the Be 1s on the Be(0001) surface.

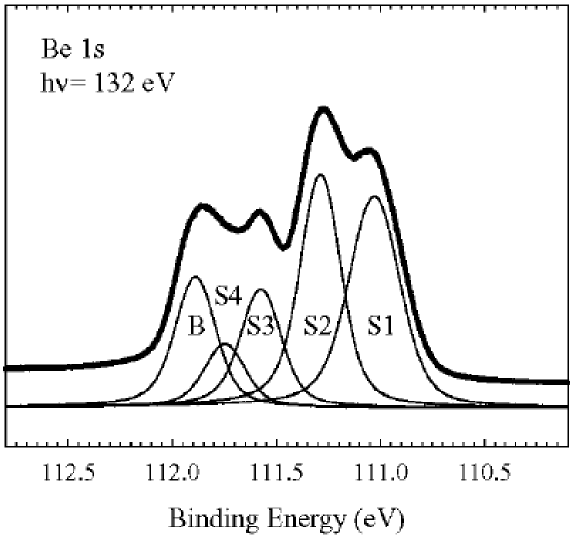

Fig 1.1 Be 1s core level spectrum on Be(0001) surface[64]

Through proper curve-fitting the five 1s core level peaks for Be(0001) are cleanly distinguished. B means peak for the bulk, S1 corresponds to the top layer, S2 is the second layer, S3 is the third layer and S4 the fourth layer although the signal is lower due to the stronger attenuation. This layer dependent core level shifts have been confirmed by theoretical calculations[118-120] This long range influence of surface is believed to be caused by the unusually low density of states at the Fermi level of Be metal and discovery of the fourth peak owe largely to the improved energy resolution for the core level photoemission spectroscopy.

Although the SCLS on flat surface has been studied extensively, the core level investigation on stepped single crystal surfaces are very rare. This is partly because the energy resolution is usually not good enough to distinguish the small binding energy difference between surface atoms with different coordinations. Also stepped surfaces were not paid much attention in the beginning. A few studies on several different metals showed quite controversial results. However with the development of nano-technology, stepped surfaces have been found to be crucial as substrates for thin film growth with anisotropy , self-assembly nanowire growth and as defect-rich substrates for catalysis, much more research has been conducted on stepped surfaces than 10 years ago. For all above important studies, it would be very important to know the atomic and electronic structure of the stepped surface , the dynamic growth of nanowires and phase transition with different temperature and chemical environment. Some dynamic processes are too fast to be observed by methods like LEED and STM and only a time-average image can be observed. Core level photoemission spectroscopy has a much faster detecting time and with the state of art third generation synchrotron or even the future free electron X-ray laser, it will gain enormous advantages over other surface science experimental methods. As an example for recent years' surface core level shifts on stepped surfaces, J. Gustafson et al. studied Rh(553) and Rh(15 15 13) surfaces with high resolution surface core level photoelectron spectroscopy. [8]They can distinguish the step edge atoms and underlayer atoms from other surface atoms with distinct Rh $3d_{5/2}$ peak from the step edge. They can also show the initial stage of surface oxidation (the oxygen adsorption site) by observe the change of the step edge peak.

Here we will focus on the stepped W(110) surface that we believe can serve as a very good substrate for thin film and nanowire growth due to its high surface energy and elevated melting temperature. Although there are not many data from the stepped tungsten surfaces, there are many examples of flat W(110) surface serving as a high quality substrate, promoting us to focus on its vicinal siblings. For example, Fe can show layer by layer growth on W(110) and W(100) surfaces up to four monolayers. The Fe films on the tungsten surface can be a good model to study two dimensional magnetic phase transition.[2-4] Also , quasi one dimensional Fe patches can form on step W(110) surface (very small vicinal angle, however). The quasi one dimensional Fe patches show substantial magnetism. W(110) has been used as a substrate more often than W(100) because W(100) surface is unstable in phase when the temperature is below RT [1] .

Research on stepped tungsten surfaces with large vicinal angle(more than 2 degrees) has still not touched by many people. The core level line shift study on W(320) is one of the few examples. However, there were significant differences between different research groups and between theory and experiment [5,6,7] On a stepped surface, there are different types of atoms associated different surroundings, namely, the step edge atoms, the terrace atoms, the base and corner atoms. These different types of atoms have different coordinations (here we consider not only the nearest neighbors) thus could have different binding energies. The idea scenario is photoemission spectra give at least four distinct peaks. So far nobody has achieved that yet. Possible reasons include not good enough instrument and photon resolution for the very small shifts, or possible surface relaxation. Then we have to lower our expectation. Among those different types of atoms, the step edge atoms are most interest because experiments showed many adsorption and reaction process happen on the step edge. If the stepped surface does not have relaxation or reconstruction, the atoms on the step edge should have a smaller binding energy compared to the atoms at the flat terrace part because of smaller coordination number and this different should be larger than the binding energy difference between different rows on the terrace. However , previous experiments failed to give a reliable result because of low energy resolution and possible contamination.

There are two types of vicinal W(110) surfaces that have been studied for film growth(for very small vicinal angles). One is with step parallel to [001] direction, the other with step parallel to [1-1 0] direction. Experiments show step orientations play a very important role on film growth and magnetic behavior for Fe nanostripes growth[10]. On a vicinal W(110) surface with step edge along [001] direction, uniform quasi one dimensional patches can be formed. On the other hand, if vicinal W(110) surface with step perpendicular to [001] direction is chosen, only three dimensional islands can be found.[10]. For W(320), W(540) , the step edge is along [001] direction while the step edge is along [1-1 0] for W(331), W(551). The latter have been studied with LEED and angle-resolved photoemission(ARPES) in recent years. And core level line shift investigation of Au adsorption on oxidized W(331)/W(551) for catalysis study was reported last year. I will talk about Shikin et al's LEED and ARPES study in this section as complimentary methods for electronic structures and nanowire growth.

Low energy electron diffraction can show split spots associated with the corresponding vicinal angle, thus can tell the information about step density and orientation. It also can display different reconstructions associated with nanowire growth. Angle resolve photoelectron spectroscopy (ARPES) will let you know the electronic structure and surface band structures. For different stepped surfaces with different step orientation and different vicinal angles, the band structures could be quite different. A.M. Shikin et al did ARPES on several different stepped W(110) surface[9]. Fig 1.1 shows the ARPES spectra along and perpendicular to the steps of clean W(331). There is strong d band dispersion in both directions compared to flat W(110) surface. By comparing with LEED experiment at different electron energies and using theoretical calculation, they concluded that final state effect due to the superlattice formed by the steps play a key role on the dispersion along the direction perpendicular to the steps. This kind of dispersion is different from band structure caused by the periodic arrangement of step edge atoms along the direction perpendicular to the steps. That means we cannot see apparent interaction between adjacent step edges. This is very important for nanowire growth on the stepped W(110) surface because we don't want interaction between different wires.

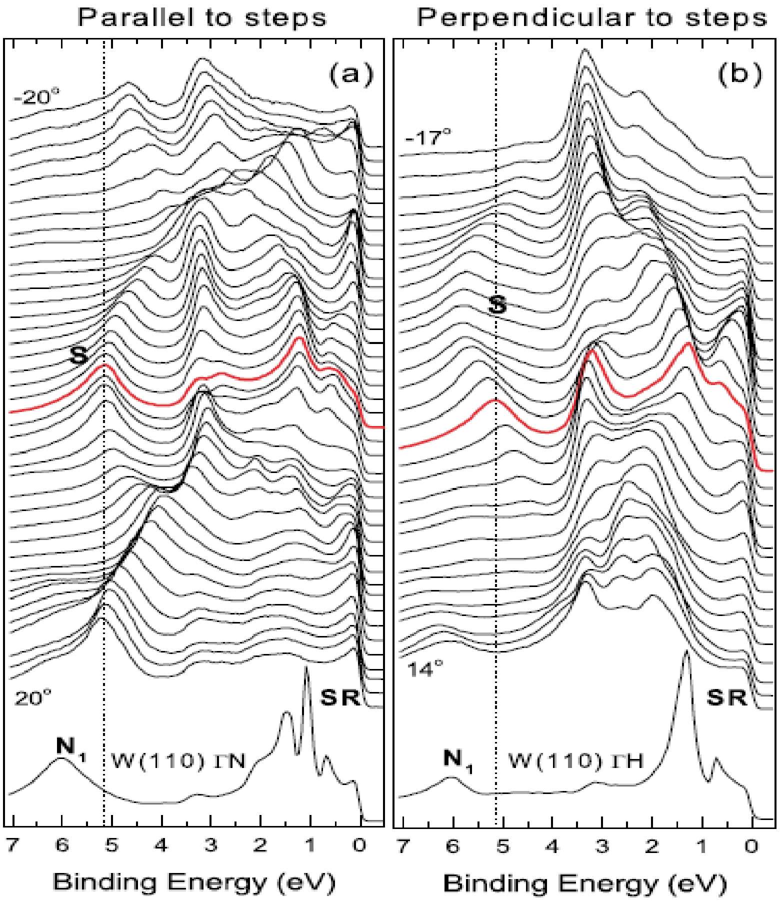

Fig 1.1 Angle-dependent photoemission spectra of W(331) parallel (a)and perpendicular (b) to the step direction for 62.5 eV photon energy.[9]

1.2 Stepped surface used as one dimensional defects for catalysis

Stepped surfaces can also be used as template to support nanometer scaled structures which could enhance catalysis of certain chemical reaction. One very important reaction is the oxidation of CO because of large amount of exhaust produced by industry. Recently it was reported that unprecedentedly high catalytic activity was observed for the 1x3 reconstructed Au bilayer on TiO_2 in CO oxidation.[21,22] The achievement of high catalysis is due to enhanced chemical processes promoted on a defect-rich surface. For stepped surface, the step edges could be used as a large number of one dimensional defects arranged periodically. If noble metals such as Au or Ag are grown on the oxidized stepped surface, the noble metal particle can be oxidized efficiently. The core level line shape and shift by photoemission can help to check the oxidization situation. This was demonstrated recently by A. Varykhalov et al on certain stepped tungsten surfaces. [25] They used W(331), W(551), W(145) precovered by oxygen and achieved complete oxidation of adsorved Au. Thus the experiment established the role of atomically scaled surface defects as chemical reaction centers.

Fig 1.2 shows Au 4f core level photoelectron spectra for submonolayer Au deposited on preoxidized vicinal W(110) surfaces. All of the spectra presented are decomposed into their spectral components. Spectra plotted with open circles(mark I) were measured from “ as deposited” Au. Those plotted with filled circles (mark II) were recorded after annealing at 900K. We can see that after annealing the sample at 900K, Au spectrum on the W(331) surface has significant change with increased intensity at the highest binding energy. At the same time, other peaks with lower binding energies disappeared completely. So one can guess at this moment the Au is oxidized , at least mostly. On the other hand, this effect is not so obvious on the W(110) and W(145) surfaces.

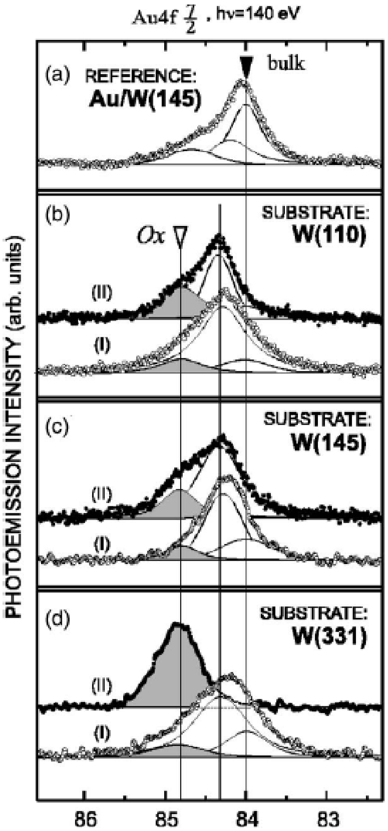

Fig 1.2. Photoemission from Au 4f7/2. (a) Reference spectrum of 2-ML-thick Au on clean W(145). Panels (b)-(d) display spectra from 0.5 ML Au on (b) preoxidized flat W(110), (c) oxidized W(145), and (d) oxidized W(331). [25]

In order to verify the Au oxidation assumption, W 4f photoemission spectra are also measured. Fig 1.3 shows the result. We can see that the higher binding energy peaks for W(331) decrease greatly and a lower binding energy peak appears. There is also a shift to lower binding energy for those high binding energy peaks. This implies weakening of O-W chemical bonding as a result of a change in coordination of O atoms relative to the W substrate. By combining the results from both Au and W core level spectra, they conclude the switching of the oxidation state from W to Au.

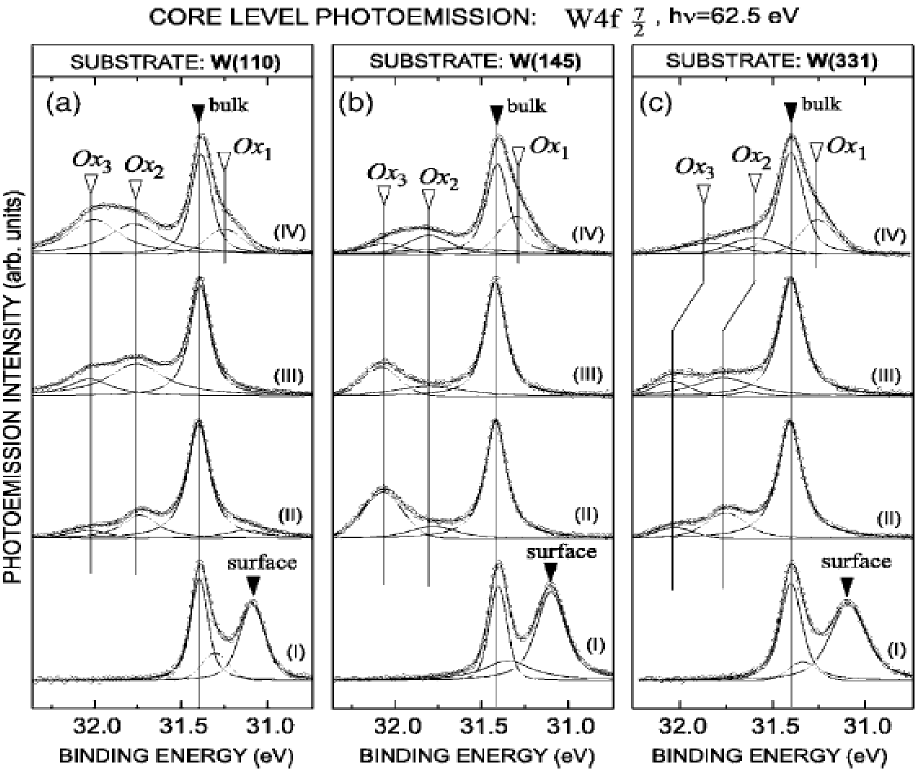

Fig 1.3 Characterization of the chemical state of W by photoemission from the W 4*f*7/2 core level. Panels (a), (b), and (c) present spectra from W(110), W(145), and W(331), respectively. Roman numerals near each spectrum denote different stages of the sample preparation: (I) clean surface, (II) oxidized sample with *p*(2x1) superstructure of oxygen, (III) oxidized substrate with a submonolayer amount of Au "as deposited" at room temperature, and (IV) sample with Au oxidized by annealing at 900 K. [25]

1.3 Core level photoemission study on nanowire growth on stepped surface

With surface core level line shape and shift studies, people can investigate phase transition and dynamic process for nanowires at substrate at different temperatures and chemical environments . LEED and STM have big limitation in this area because of their longer time scale of measurements and inability to distinguish elements. Photoemission has a much shorter scales and very capable of dealing some types of phase transition. For example, Si(111)-In has 4x1 and 8x2 phases at different temperatures and they both display nanometer scale In wires on the Si substrate. The phase transition temperature is between 90 and 125K. The 4x1 phase is above 125 K and metallic while the 8x2 phase is below 90 K and behave as an insulator. It has been unkown for many years on what happens during this phase transition temperature range. Many research groups are trying to find the dynamic process for this phase transition process. González et al. introduced a structure model for the LT phase and explained the RT phase as a dynamically fluctuating one between the degenerated 8x2 LT structures.[13] They believed above Tc there is a intermediate metallic state between two different 8x2 configurations. The room temperature metallic phase is formed by more and more occupation of the intermediate state for higher temperature. Ahn et al. recently studied In and Au on flat and stepped Si(111) surfaces.[12]. They measured temperature related Si(111) 4x1 to 8x2 phase transition with both valence and core level PES and they found solid evidence against Gonzalez’s theoretical work.

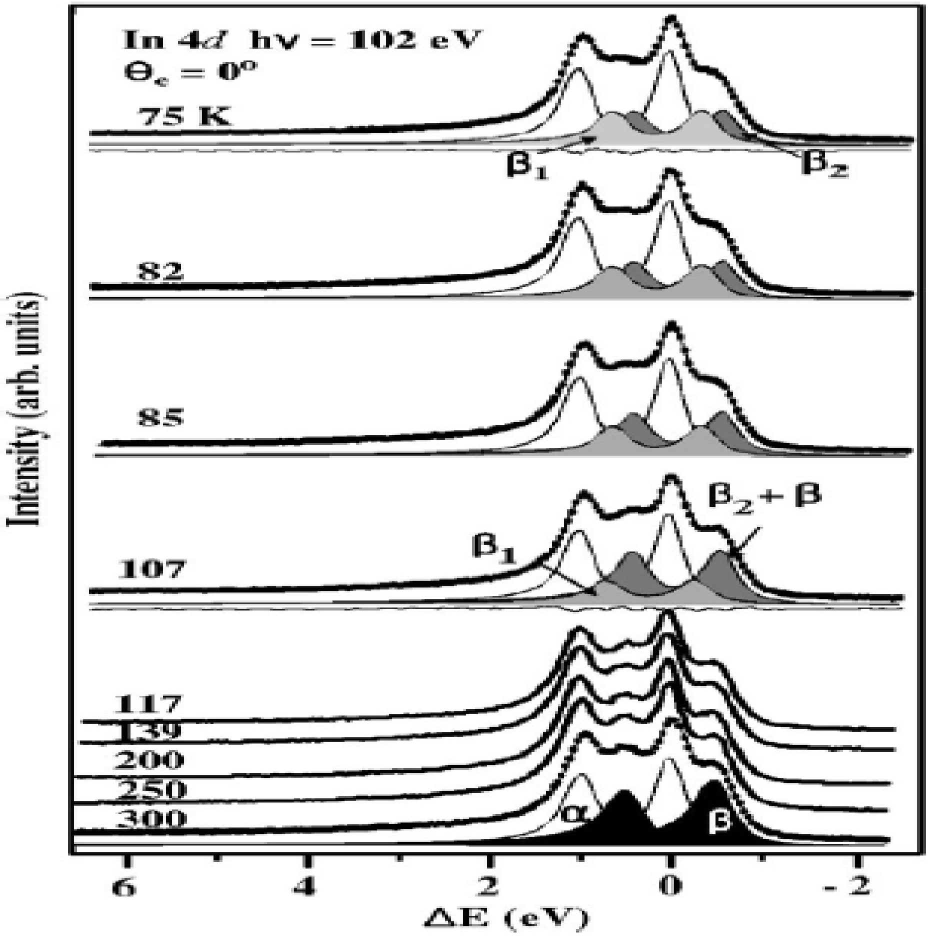

Fig 1.4 Temperature dependent In 4d photoemission spectra measured at the normal emission with a photon energy of 102 eV. The decompositions through standard least-squares curve fittings using asymmetric Doniach-Sunjic line shapes are given together. The fitted data (dots) are overlaid with the results of the fits(thin solid lines). [14]

Fig 1.4 shows the In 4d core level photoelectron spectra which can reflect instantaneous local charge distribution on In atoms. The spectra are being curve-fitted by Doniach-Sunjic line shape. In the figure, the temperature decreases from bottom to the top. At the bottom is the spectra at RT , corresponding to the 4x1 phase. The spectra can be well fitted with two components α (white area) and β (shaded area) . Both α and β peaks are asymmetric indicating metallic feature of the phase. The energy difference between the two components is 0.50 eV was attributed to two different In sites. The two sites are related to two different In chains, the inner and outer chain with a unit wire.[14] The outer In chain has a smaller binding energy and corresponds to the α component. From room temperature to Tc, there is not very much change for the In 4d line shape. However, the line shape of β component changes quite a bit when temperature changes within the low temperature phase. Actually β component divided into two components (β1 and β+β2). The systematic change between β , β1 and β+β2 at only temperature below Tc strongly suggests that there is no such two 8x2 fluctuation above Tc. This conclusion cannot be achieved by STM or LEED because the dynamic scale is too short and STM and LEED are too slow.

1.4 Nanowire growth on stepped metal surfaces

One dimensional metallic nanostructures are one of the most promising materials in the future technology. Circuits or sensors as small as a few nanometers will be likely to replace today’s bigger size devices. The new devices will have higher efficiency or capacity and bring a completely new idea to the industry. Extensive research has been conducted in this area to understand the mechanisms of nanowire growth, material structures and properties. Traditional lithography becomes more difficult for smaller structures and an infinite chain of atoms freely suspended in space is nearly impossible to produce experimentally. An alternative way to produce nanowires is to use a stepped surface as a substrate. In the appropriate temperature range, deposited atoms adsorb preferentially on step edges and their mobility along the edge is enhanced, these are crucial preconditions for the uniformity of the nanowires. This widely applicable technique permits the preparation of large-area nanostructured samples of outstanding quality and, moreover, one of the important structural parameters, the interwire distance, can be tuned simply by changing the miscut angle. With the powerful third generation synchrotron radiation source, it is possible to study the details of electronic structure around Fermi level and many exotic phenomena predicted by theory can be verified. For detailed development of nanowire growth on metal surface, see the Appendix.

Chapter 2

Photoemission theory and experimental methods

2.1 Sample cleanness and ultra-high vacuum

All our measurements are conducted in ultra-high vaccum (UHV) systems. The surface science had been developed very slowly until UHV was achieved in 1950s. Surface physics is dealing with structures with only a few atomic layers and quite often probing intrinsic physical properties such as atomic distances, crystal symmetry, or electronic structure . Only 10% coverage of hydrogen on a metal surface could change the surface relaxation by amount that can be easily detected. Basically under 10^{-6} Torr pressure, one monolayer contamination can form in a second. This assumes a sticking coefficient near unity and a long sticking time. Many surface experimental methods like LEED , STM requires relatively long time (up to one hour) to record raw data. Thin film , nanowires and nanodots growth also could take tens of minutes or longer. In order to keep relatively clean surface for over an hour, 10^{-10} Torr base pressure is a minimum requirement. At his pressure, the primary residual gases are H_2 and CO. They can form a monolayer on a clean surface in a few hours. So constant flashing every few hours is needed to guarantee the cleanness of the sample. The cleanness of sample can be easily checked by Auger electron spectroscopy.

2.2 Electron spectroscopies

Compared with X-ray, electron has smaller mean free path thus has a smaller escape depth in a solid. Fig 2.1 gives a universal curve for the mean free path for electrons. An experiment using electron spectroscopies is usually surface sensitive . For example, both low energy electron diffraction (LEED) and Electron energy loss spectroscopy (EELS) electrons have a escape depth of 0.5nm, Auger electron spectroscopy (AES) electrons have a escape depth of 1nm and for photoemission spectroscopy , the value is 0.5 to 2nm depending on the photon energy. Ultra- violet phonons have energy smaller than 150 eV and are best to be used to investigate band structures and shallow core level states. X-ray is good for deep core level study and is often quite useful for structural and local chemical environments investigation. Another advantage is of electron spectroscopy is that it is easy to focus electrons, especially with today's state of art electrostatic lens. Electrons are also easy to be detected and energy and angle resolved by an analyzer. For example, a 200mm Scienta can measure electrons with sub-meV energy resolution and better than half degree angular resolution. However there are also some disadvantages of electron spectroscopies. First, very high vacuum are usually needed.(For example, LEED needs at least 10^{-8} Torr vacuum). And also, it is often difficult to separate information from the surface and from the bulk due to a small escape depth for electrons.

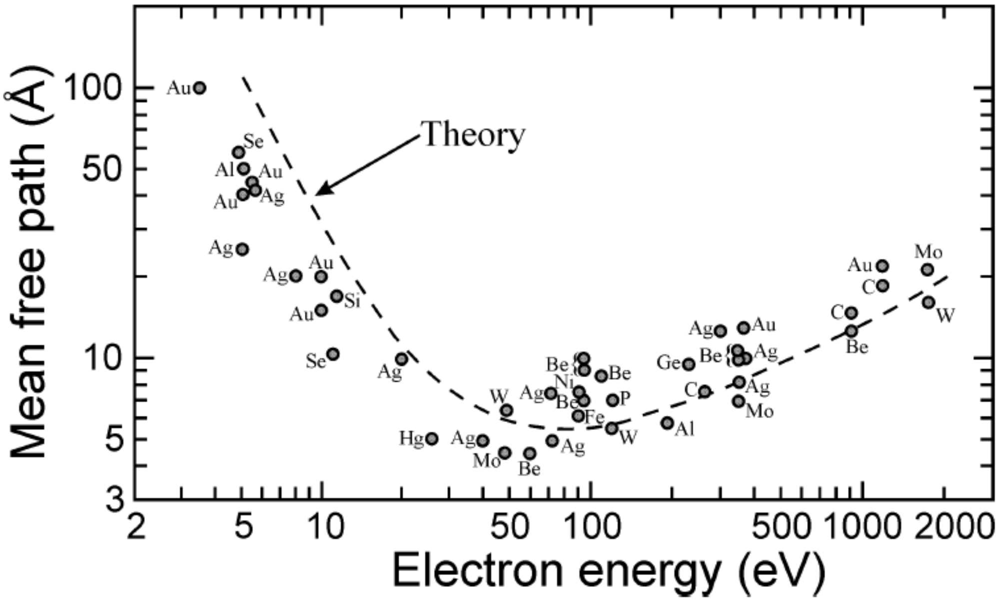

Fig 2.1 The universal curve of electron mean free paths. [80]

2.2.1. Photoemission spectroscopy

Photoelectron spectroscopy generally includes all the techniques based on the photoelectron effect discovered by Hertz. Einstein explained the effect by using quantized light (photon). Basically when light is incident on a sample, an electron can absorb a photon and escape from the material with a maximum kinetic energy, hν - Φ, where hν is the light energy and Φ is the work-function of the material. Thus photoemission spectroscopy can be used to investigate occupied states in a solid. While the momentum of electron parallel to the surface is conserved, the momentum perpendicular to the surface is not conserved. Therefore, angle-resolved photoemission is ideal for 2D materials where the principle momentum directions of interest are parallel to the surface.   For the unoccupied states in a solid, inverse photoemission can be used. But the intensity of spectra and resolution cannot compare with photoemission spectroscopy.

In practice, the electrons ejected from the material are collected using a hemispherical analyzer in which a series of electrostatic lens focus the electron onto a entrance slit. Upon electrons with certain energy passing through an exit slit, a single channeltron or a two-dimensional (energy, momentum) multi-channel plate can multiply the electron pulse. Finally a multichannel analyzer can record the counting rate versus kinetic energy spectra. The sample and the detector are kept in an ultra high vacuum (UHV) chamber in order to minimize surface contamination.

2.2.2 Low-energy electron diffraction (LEED)

Low-energy electron diffraction (LEED) is a major technique for the determination of surface structures. Actually during the past three decades, LEED solved 70% of the surface atomic structures that have been determined. LEED is also a convenient and easy method compared with many other surface science tools. When installed on a UHV chamber, it may be used in one of two ways :

1. Qualitatively : where the diffraction pattern is recorded and analysis of the spot positions yields information on the size, symmetry and rotational alignment of the adsorbate unit cell with respect to the substrate unit cell. It is faster and much easier than a real space atomic topology measurement device like STM. But it

doesn’t have the ability to detect local arrangement of atoms. Like STM, it cannot distinguish different elements.

2. Quantitatively : where the intensities of the various diffracted beams are recorded as a function of the incident electron beam energy to generate so-called I-V curves which, by comparison with theoretical curves, may provide accurate information on atomic positions. Most of the surface structures were determined by this way. Kinematic and multiple scattering theories may be used to try and understand the variation of LEED spots with energy. The major disadvantage of this method is that you have to use trial-and-error calculation for many cycles, especially time consuming for the dynamic LEED which considers multiple scattering.

Fig 2.2 shows a LEED system

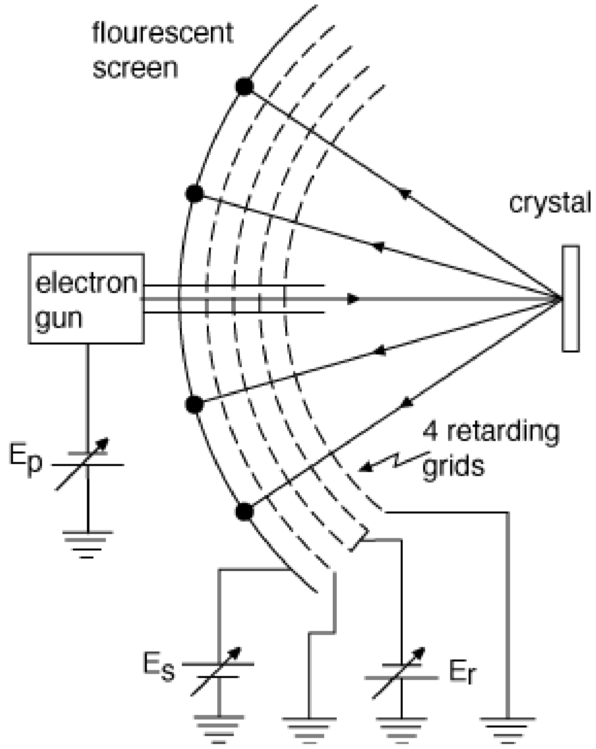

Fig 2.2 A diagram for the LEED system[85]

The crystallographic quality of the sample may be measured to within the limits of the LEED system. The coherence length of electrons from the LEED electron gun is one limiting factor. A smaller spot-size with corresponding little divergence or convergence and narrower energy spread will give a greater coherence length. A better coherence length allows for better examination of the spot-profiles of different LEED beams. The energy of electrons at a minimum must be large enough so that their de Broglie wavelength is comparable to of the atomic spacing. A surface lattice may be described by primitive direct lattice vectors $\mathbf{a}_i$ and reciprocal lattice vectors $\mathbf{b}_j$ such that

$$\mathbf{a}_i \cdot \mathbf{b}_j = 2\pi\delta_{ij}$$

LEED occurs when incident and scattered electrons satisfy the Bragg condition:

$$(\mathbf{k}_i - \mathbf{k}_f)\cdot\mathbf{b}_{surf} = 2\pi n$$

where n is an integer. LEED can be represented by an Ewald construction. Reciprocal lattice rods described by $\mathbf{b}_{surf}$ intersect a sphere of radius $|\mathbf{k}_i| = |\mathbf{k}_f|$. Normally, $\mathbf{k}_i$ is described by a rod (00) and $\mathbf{k}_f$ will intersect the sphere at the point of another $\mathbf{b}_{surf}$ reciprocal lattice rod. The intensity and the number of states connecting k_i to k_f changes when the final energy changes. In a similar way, the intensity variations versus energy may occur in photoelectron spectroscopy. Fig 2.3 shows the Ewald sphere construction in the LEED.

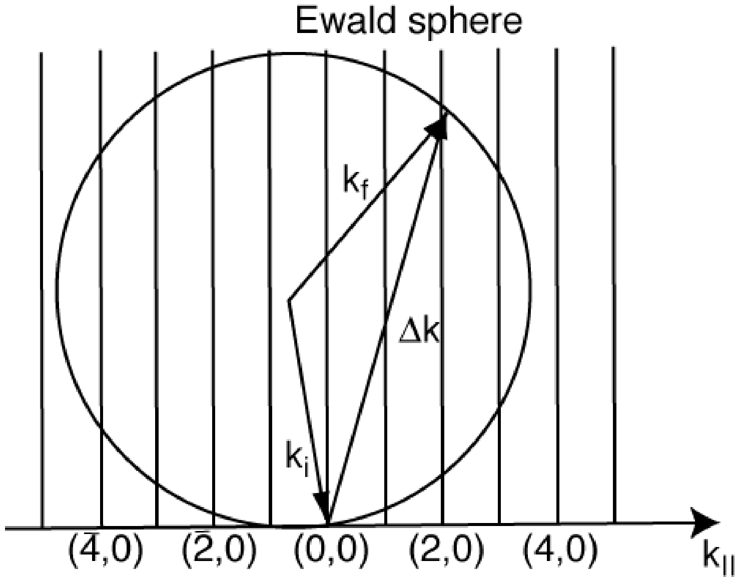

Fig 2.3 The Ewald sphere construction in LEED

2.2.3. Auger Electron Spectroscopy (AES)

In order to detect contaminations on a surface or check the composition of adsorptions or surface structures, Auger electron spectroscopy (AES) is often used. In AES, an electron with kinetic energy of several keV are incident on the surface, causing a core electron to be ejected outside the sample. The unoccupied state will soon be filled by an electron from a core state with higher energy. The energy released by this transition will give to a third electron at the same initial shell as the second one. This third electron is called Auger electron. The Auger electrons could be detected by an electron energy analyzer if they are from the atoms close to the surface and are able to escape to the vacuum. The energy of the Auger electron can be written as $E = (E_1 – E_2) – E_3$, where $(E_1 – E_2)$ is the potential energy difference between the initial states of the first and second electrons and E_3 is the binding energy of the third electron. Each element will have unique energies of E_1 , E_2 and E_3, thus the Auger spectra can distinguish different elements on the surface except hydrogen and helium which have less than three electrons. Helium is not a problem because it would not stick on a surface at conventional temperatures (i.e. , > 77 K) even if present. Hydrogen, on the other hand , is one of the main residual gases in a UHV chamber. Furthermore, Hydrogen is hard to be romoved from the chamber and it can stick on many surfaces and cause surface relaxation or reconstruction. In addition, Auger electrons usually have kinetic energy of 1 keV or less where the mean free path is small(a few nanometers). Thus, AES is inherently a surface sensitive technique. AES signal is usually very weak and a lock-in amplifier is needed to increase the signal/noise ratio.

2.3 Photoemission General Theory

The photocurrent in the photoemission spectroscopy is caused by the excitation of electrons from the initial states $1/_{\mathrm{i}}$ to the final state $1/_{\mathrm{f}}$ by the photon field having the vector potential Á. The transition rate *w* can be expressed as

$$\mathrm{w} \ \mathrm{o} \ \mathrm{e}\frac{2\mathrm{rr}}{\mathrm{h}} \mathrm{l}\langle 1/_{\mathrm{f}}|\mathrm{H}^{1}|1/_{\mathrm{i}}\rangle \mathrm{l}^{2} \mathrm{o}(\mathrm{E}_{\mathrm{f}} - \mathrm{E}_{\mathrm{i}} - \mathrm{hw}) \qquad (2.1)$$

This is the so called Fermi's Golden Rule. It assumes the perturbation from the photon H^{1} is small and dipole approximation is applied. [81]

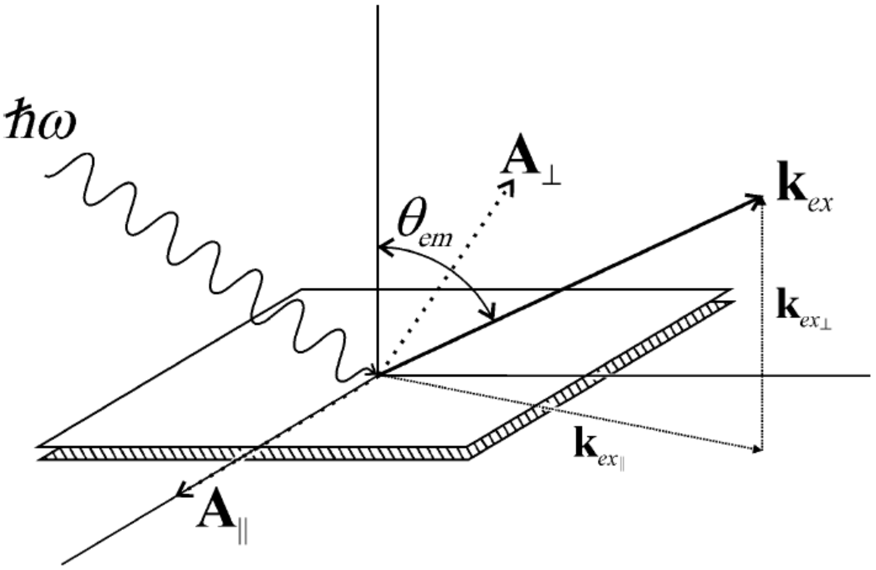

Fig 2.4 Schematic view of angle-resolved photoemission process.[114]

The perturbation H^{1} to the system can be expressed as

$$H^1 = \frac{e}{2mc}(\quad \cdot \acute{A} \quad \acute{A}\cdot \quad) \qquad (2.2)$$

is the momentum operator of the photon. The scalar potential is set to zero in this case. If the Coulomb gauge is selected for $\acute{A}$, then $\bigvee' \cdot \acute{A} = 0$, thus the perturbation can be

written as

$$H^1 = \frac{}{me} \quad \cdot \acute{A} \qquad (2.3)$$

The transition rate then becomes

$$w \; o \; e\frac{2rre}{hmc} l\acute{A}\cdot <1/_f l \quad 1/_i)l^2 o(E_f - E_i - hw) \qquad (2.4)$$

Here the dipole approximation is applied thus $\acute{A}$ is treated as a constant vector. The maximum rate of the transition happens when

$$E_f - E_i = hw \qquad (2.5)$$

The above analysis is based on electron gas or local atom environment. For a solid crystal, the photoelectron has to overcome work function to get to the vacuum. Outside the crystal, the kinetic energy of the electron E_{kin} can be expressed as

$$E_{kin} = hw \quad E_i - e<j \qquad (2.6)$$

$e\Phi$ is the work function of the crystal. The kinetic energy of the electron outside the crystal can be measured by an analyzer. The work function can be determined by the photoemission spectra. So the binding energy of the electron inside the crystal can be obtained if no final effect happens during the process. The photoemission process can be divided in three steps by Berglund and Spicer's *three-step model*.[82, 84]

The first step is the optical excitation of an electron inside the crystal. In this step, generally a direct transition happens(no phonon participates in) So the wave vector for the initial and final state $\vec{k}_f = \vec{k}_i$. This process can be illustrated by Fig. 2.5.

The second step is the propagation of the electrons to the surface. During this step, most of the electrons are scattered inelastically. If the escape depth is d, then number of electrons reaching the surface would be equivalent to the number of electrons that have transition in a layer with thickness of d. Those electrons lose part of their energies and thus they don’t carry the initial state information. They will finally become the secondary electron background in the photoemission spectra.

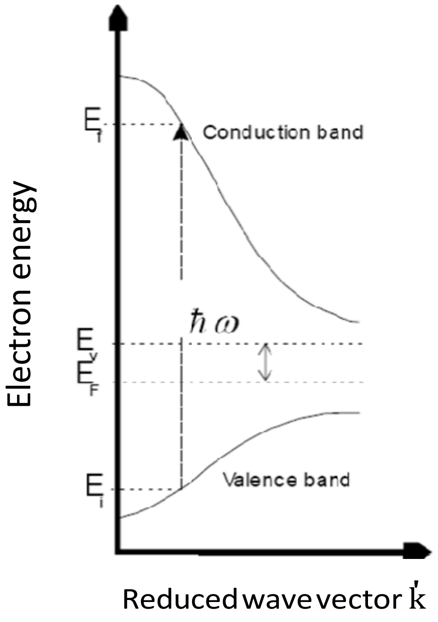

Fig 2.5 Optical excitation of the electron from initial state band to final state band.

The third step is the escape of the electron into the vacuum. During this step, some of the electrons will be reflected by the surface while others penetrate the surface and emit out. The wave vector perpendicular to the surface $k_{1-}$is not conserved due to symmetry breaking. This is a major factor that limit the photoemission spectra as a tool for 3D band mapping for a solid. The wave vector parallel to the surface must be conserved by momentum conservation law, thus

$$k'_{xt} = k'_{int} \quad ' \qquad (2.7)$$

Outside the crystal, there is only kinetic energy for the electrons, it is

$$E_{kin} = \frac{h^2 k^2_{xt}}{2m} = \frac{\underline{h}^2}{2m} [k^{2}_{xt1-} \quad k^2_{xt}] = E_f - E_{vae} \qquad (2.8)$$

E_{vae} is the barrier potential at the surface. It has a relation with the work function as

$$e<j = E_{vae} - E_F \qquad (2.9)$$

E_F is the Fermi energy. If we defined the binding energy for the initial state before photon excitation is E_B, then $E_B = -E_i$ (E_B is defined as a positive value). The wave vector outside the crystal can be expressed as

$$k_{xt} = J\overline{\frac{2m}{h^2}(hw - E_B - <j)} \sin\{\} = J\overline{\frac{2m}{h^2} E_{kin}} \sin\{\} \qquad (2.10)$$

$$k_{xt1-} = J\overline{\frac{2m}{h^2}E_{kin} - ('_{int} \quad ')^2} = J\overline{\frac{2m}{h^2} E_{kin}} \cos\{\} \qquad (2.11)$$

θ is the emission angle for the photoelectrons. If we put an analyzer outside the sample, θ will be the angle between the sample normal and analyzer. We can change the emission angle by rotating the sample or rotating the analyzer. Thus by sweeping the angle θ to a certain range with small angle steps, we can get the relation E_{kin} vs k , thus E_B vs k through Eq 2.10. In this way , we get the 2D band structure for surface electrons. Analyzer rotating can let you investigate more regions in the Brilouin zone, but it is not convenient for a big analyzer to rotate. So the resolution is limited. So most of today's high resolution angle resolved photoemission experiments are done with sample rotating.

However, to get 3D band structure by photoemission method is not an easy thing. The perpendicular component of the wave vector is not conserved so we don't know exactly what the 3D state inside the surface. A simple way is to assume free electron parabola for the final state. From the free electron model and from Eq 2.6, we can know that if the momentum parallel to the surface is conserved, the momentum perpendicular to the surface will be dependent on the photon energy. So by doing photon energy dependent photoemission and through complicated calculation, we can get the 3D band structure.

2.4 Core level photoemission study Doniach-Sunjic lineshapes

For core-level photoemission, the electrons are emitted from localized states . There is no band dispersion associated with the initial state. So the binding energy is not affected by θ [83]. However, the matrix element lȦ · <1/$_f$l l1/$_i$)l in Eq 2.4 is a function of θ , thus transition rate depends on θ. So the intensity of the photoelectron spectra is dependent on θ. Also, different local chemical environment will give different local valence electron distribution. For example, the neighborhood of Al atom in the Al_2O_3 is different from the Al atom in an Al metal. Thus the wave functions will be different. The valence electrons change will affect the binding energy of the atom through Coulomb interaction. This causes a chemical shift of the core level peak with respect to the pure Al case. So core level photoemission spectra is a very powerful way to acquire chemical environment and bonding structure around a specific atom. However, photoemission produces a final state that is one electron short of the initial state. So the only after some theoretical considerations can we relate the final state (the measured state) to the initial state. The emitted electron will have an interaction with the core hole generated by the excitation. For this case, Doniach and Sunjic made a very successful theory that fits the experiment very well.[86]

When an core level electron is excited by a photon and emitted from the atom, there is a core hole left. The core hole will attract the emitted electron thus a electron-hole pair formed. If the energy of the hole state is E_h and the initial ground state energy of the metal is E_g, then the measured kinetic energy of the photoelectron will be

$$E_{kin} = hw - <j \quad (E_g - E_h) \qquad (2.12)$$

<j is the work function and hw is the photon energy. So there is a energy difference between the initial and final state. Since $(E_g - E_h)$ �0, the maximum of the measured photoelectron energy will be hw – <j. The energy below this maximum corresponds to events in which the hole + Fermi sea is left in an excited state. If the hole density is low,

we can neglect the hole-hole interactions. The remaining electrons will reorganize to screen out this Coulomb field caused by the hole. The lowest electron-hole pair energy has the highest probability to be created. This will cause the number of photoelectron decreases with the decrease of kinetic energy. If we don’t consider the effects that cause the broadening of the peak, the photoelectron spectra for that core level state will be like curve A in Fig 2.6

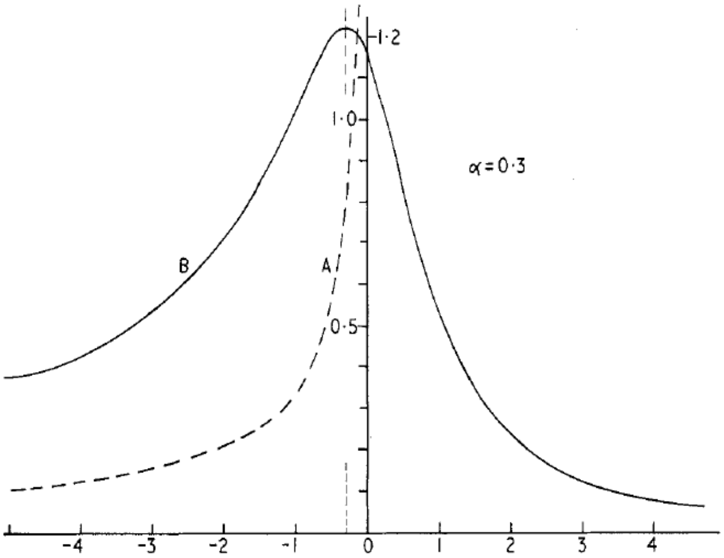

Fig 2.6 Singluar line shape for singularity index α = 0.3 for curve A, in the absence of lifetime broadening. Curve B is the result that finite core hole lifetime is considered. From Ref [86]

If the electron-hole pair life time is considered, there will be an intrinsic line width. Then the peak will become curve B. So the lineshape of the core level peak will change from a δ function into an asymmetric Lorentzian function, the so called Doniach-Sunjic lineshape [86]. The level of asymmetry can be defined by the singularity index, α. Doniach and Sunjic derived the photoelectron yield function as

$$Y(€) = \frac{\Gamma(1 - a)}{(€^2 \quad y^2)^{(1\text{-}a)/2}} \cos\left(\frac{rra}{2} \quad ()(€)\right) \qquad (2.13)$$

Where $()(€) = (1 - a)\tan^{-1}(\frac{€}{y})$, γ is the lifetime width of the state. € is measured relative to the maximum energy in the absence of lifetime broadening. Fig 2.5 shows the lineshapes with different value of singularity index.

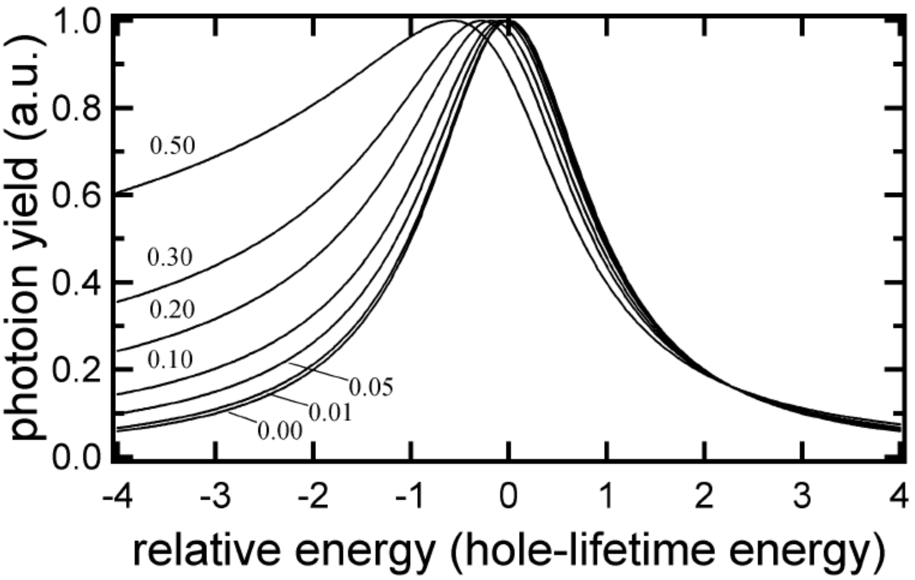

Fig 2.7 Doniach-Sunjic lineshapes for different values of the singularity index α before convolution with instrumental response or phonon broadening terms.[114]

In practice, lattice vibration and instrumental resolution can also cause a broadening for the core level peak. This kind of broadening can be described as a Gaussian function. In fact convoluted Doniach-Sunjic lineshape with a Gaussian broadening fits experiments very successfully.

2.5 Electron energy analyzer

Today’s extremely high resolution photoemission owes a lot to the improved design of electron energy analyzer. The most common analyzers in use are electrostatic analyzers: the cylindrical mirror analyzer (CMA) and the hemispherical mirror analyzer (HMA).

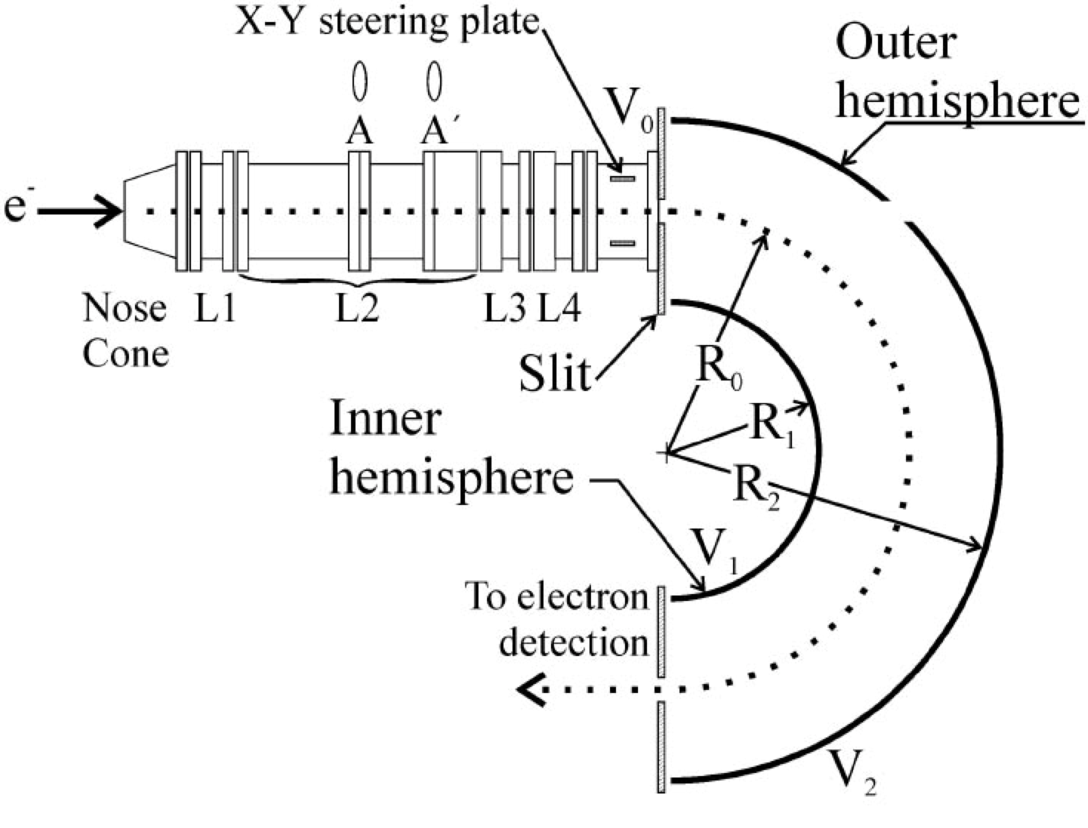

Fig 2.8 HA 150 analyzer and lenses system.[116]

Fig 2.8 shows a VSW HA 150 hemispherical analyzer and the lens system . A lens assembly with four electric lenses is used to transfer electrons from the sample to the entrance slit. The electron optics in the lens assembly has an element that retards or accelerates electrons of a certain energy to the pass energy. In a hemispherical analyzer, an electrostatic field is applied between an inner and outer hemisphere. Electrons with only certain energy (pass energy E_0) pass through both the entrance slit and exit slit to the detector. The path of the electrons is a circular trajectory on the median hemispherical surface. The VSW HA150 has a mean radius R_0 of 150mm. The voltage ratio of the inner hemisphere to the entrance slit and of the entrance slit to the outer hemisphere are 16/9. [114]If we assume the voltage on the entrance slit is V_0, then the potential difference between the inner and outer hemispheres is $\Delta V = (16/9 - 9/16) V_0$. The energy resolution of the HMA is determined by the radius and the width of the slits at the analyzer entrance and exit. It can be written as [116]

$$\frac{\Delta E}{E_0} = \frac{w}{2R_0} \quad a^2$$

Where w is the slit width and a is the full angle of the beam at the entrance slit. For a real analyzer, the mean radius R_0 is fixed, we can reduce the slit width and full angle of the beam at entrance slit to increase the resolution. But the output signal is also reduced. So we have to compromise between these two factors. The equation also shows the radius of analyzer should be built as large as possible to enhance the energy and angular resolution.

A cylindrical mirror analyzer (CMA) is used for Auger Electron Spectroscopy (AES) in our lab. Fig 2.9 shows a drawing for a double pass CMA. It consists of two concentric cylinders. The inner cylinder has a ground potential while the outer cylinder is at a negative potential. The electric field between the inner and outer cylinders lets the

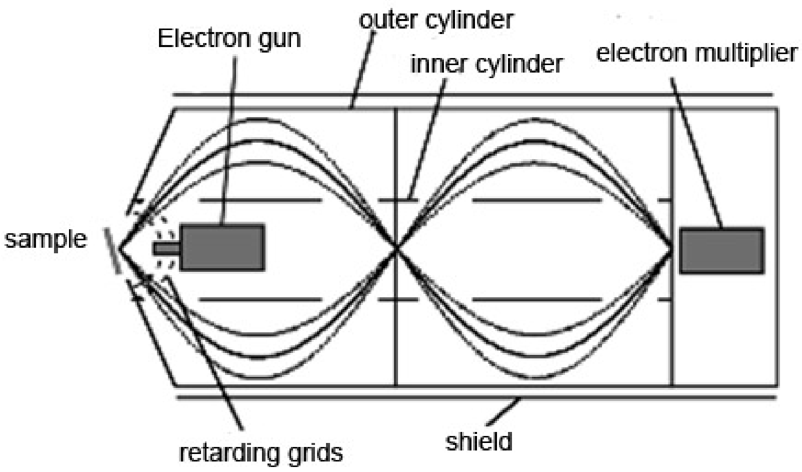

Fig 2.9 A sketch for a cylindrical mirror analyzer (CMA).[116]

electrons inside it form trajectories with a radius depending on the energy of electrons and the electric field inside the analyzer. Like the hemispherical analyzer, only those electrons with a certain energy(the pass energy E_0) can be focused onto the detector. The CMA has a annular shaped entrance aperture instead of the rectangular slit on the HA150. The annulus shape aperture can allow the polar angular width as large as 12^o without sacrificing very much of the energy resolution. So one big advantage of the CMA is large acceptance angle thus higher transmission compared with a HMA. This is very important if sensitivity is a major issue of measurement. On the other hand, the focus ability of a CMA depends strongly on the distance between the sample and the entrance aperture. This impose a big geometrical limitation on spectra measurement. For a HMA, there is no such a problem because we can put a lens assembly to focus the electrons onto the analyzer. This allows the distance between the sample and analyzer significantly larger than the case for a CMA.

2.6 Photoemission light sources

Generally photoemission light sources include discharge lamp(the gas can be He, Ne, Ar, Kr, Xe or H_2) for Ultraviolet Photoelectron Spectroscopy (UPS), Mg K_α and Al K_α for XPS and synchrotron radiation for both UPS and XPS. Recently, femtosecond laser with photon energy of 6eV was developed by D.S. Dessau et al. to do angle resolved photoemission .They achieved better energy resolution, momentum resolution and more count rates than synchrotron. However, the surface sensitivity of the very low energy photoelectron (a few eV, see Fig 2.1) is not good while the bulk sensitivity can be improved a lot. On the hard X-ray side, the “fourth generation of synchrotron” based on free electron laser is being built and the world’s first X-ray free electron laser (LCLS) will become operational at the Stanford Linear Accelerator Center (SLAC) in 2009 . This talk mostly discusses the discharge UV lamp and synchrotron.

2.6.1 The discharge lamp

For a UV discharge lamp, high voltage is used to cause electron collisions with atoms, letting the atoms excited to higher states. UV light is emitted when the atoms take a transition from excited states to lower energy states. Usually the lamp can get very hot so that water-cooling is necessary. The UV light cannot be focused by a regular optical lens so the discharge lamp uses a capillary to conduct the photon. Differential pumping is needed in the lamp in order not to affect chamber vacuum very much. The capillary needs to be cleaned or changed every few years to make sure the photon conductance is good. If there is too much contamination, some weak spectrum like HeII cannot be observed.

2.6.2 Synchrotron light sources

Synchrotron radiation is the radiation that happens when high speed charged particles move in a curved orbit. From classical electrodynamics, [54] any charged particle with relativistic speed can emit electromagnetic radiation if it is accelerated in a curved path. The synchrotron radiations facilities use electrons as the high speed particles and they are constrained in a storage ring. The spectrum of synchrotron radiations can go from infrared to hard X-ray. Synchrotron radiation started to be used since late 1960s. [55]It is the so called first generation synchrotron. It is based on high energy physics research facility. (People added a few beamlines on the storage ring.) After this, accelerators which were only used for synchrotron radiation were built in many places in world. This is the second generation synchrotron. Today the most advanced synchrotron radiation is the third generation which began in the 1990s.

The power of synchrotron radiation is proportional to the fourth power of the particle speed and is inversely proportional to the square of the radius of the path. It can be derived this way.

The radiated power for an accelerated electron can be written as

$$= \frac{2K\ ^2}{3e^3} a^2 \qquad (2.14)$$

For a non-relativistic circular orbit, the acceleration is just the centripetal acceleration, v^2/r. But for a highly relativistic electron, the acceleration will be

$$a = \frac{1\ dp}{m\,dr} = \frac{1}{m} y \frac{d(ymv)}{dt} = y^2 \frac{dv}{dt} = \quad y^2 \frac{v^2}{r} \qquad (2.15)$$

where $r = \frac{t}{y}$ = proper time, $y = \frac{1}{J1-\frac{v^2}{c^2}}$ $f3 = \frac{v}{c}$

and m is the rest mass of the particle and if γ is considered constant, the radiated power should be

$$= \frac{2Ke^2}{3c^3}\, y^2\, \frac{v^2}{r}^{2} = \frac{2Ke^2y^4v^4}{3c^3r^2} \qquad (2.16)$$

For highly relativistic electrons, the speed is almost the velocity of light, so v^4 can be treated as constant. Then the major factors that determine that loss rate is γ^4 and r^2. That means the energy loss rate for the electrons is proportional to the fourth power of the particle energy γmc^2. And, the loss rate is inversely proportional to the square of radius. This is a reason for building the accelerator as large as possible

The usefulness of synchrotron radiation (SR) is in its high brilliance, continuum of photon energies leading to energy tunability and the ability to adjust ΔE/E to obtain more flux when needed. Also the radiation is linearly polarized in the plane of acceleration (in most cases the horizontal plane). Elliptical polarization occurs for bending magnet radiation observed from above or below the midplane. The radiation is emitted in pulses of 10 - 20 psec separated by some 2 nsec or longer separation if desired.[114] The continuous light can be used to do X-ray lithography and micromachining, protein crystallography, and surface science, etc [54]

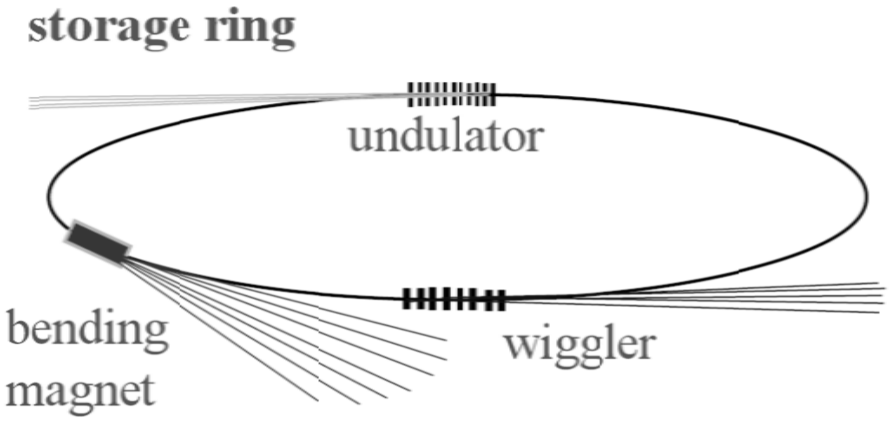

Fig 2.10 A diagram showing components for synchrotron radiation.

In order to increase radiation intensity, most of today’s synchrotrons use wigglers to shift the critical energy upwards and use undulators to coherently add radiation. These devices have great abilities to help achieve higher light brilliance and higher critical energies.

The J. Bennett Johnston Sr. Center for Advanced Microstructures and devices (CAMD) was built in mid 1990s in Baton Rouge, Louisiana. It is a second generation radiation facility and the only synchrotron in America South. At CAMD the synchrotron radiation is emitted from bending-magnets (1.48 Tesla for bend radius of 2.928 m) and a single-pole superconducting wiggler (7 Tesla) for operating conditions of 1.3 GeV of electron energy and 200 mA of electron beam current. Soft X-ray, ultraviolet and infrared beamlines are connected to the storage rings. Fig 2.11 shows the layout for the CAMD facilities. The University of Texas at Austin 6 meter TGM beamline was moved from

Brookhaven National Lab in late 1990s by Kevin Koch. The layout of the 6 meter beamline is shown in Fig 2.12. The grating monochromator consist of three toroidal mirrors, which are in charge of different photon energy ranges. The low energy grating (LEG) outputs photons energy 10-34eV. The medium energy grating (MEG) has a energy range 27 to 90 eV, and the high energy grating (HEG) has energy range from 80 to 200eV. Fig 2.13 shows the photon flux for different gratings.

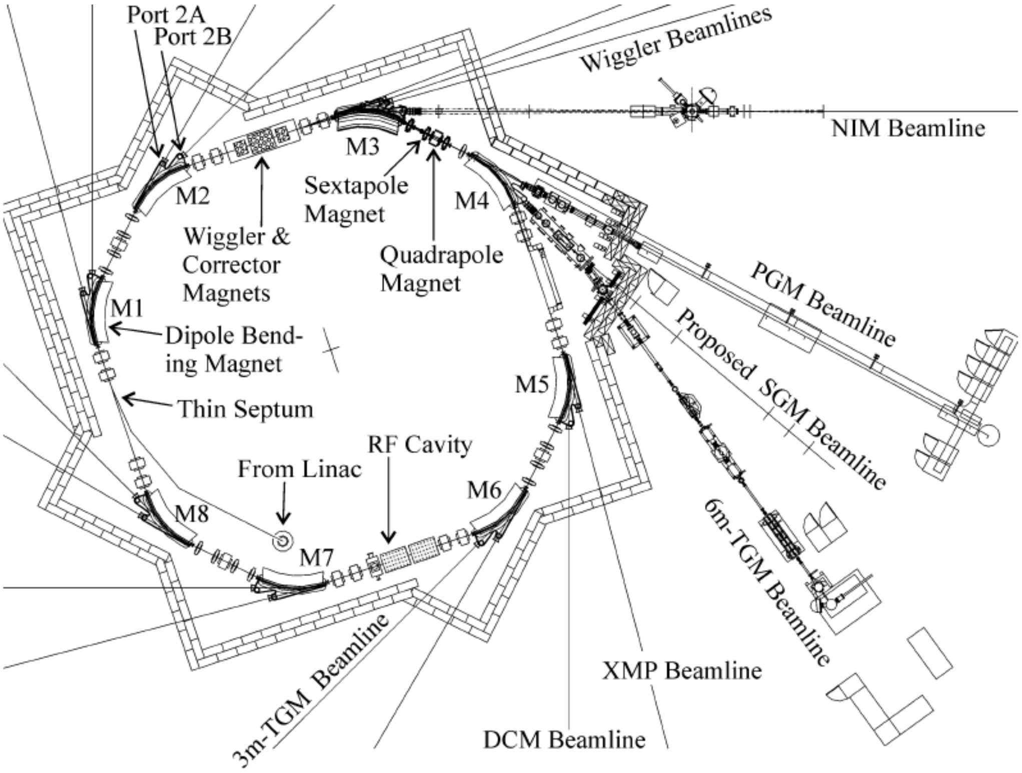

Fig 2.11 The layout of CAMD and orientation of the 6m-TGM [114]

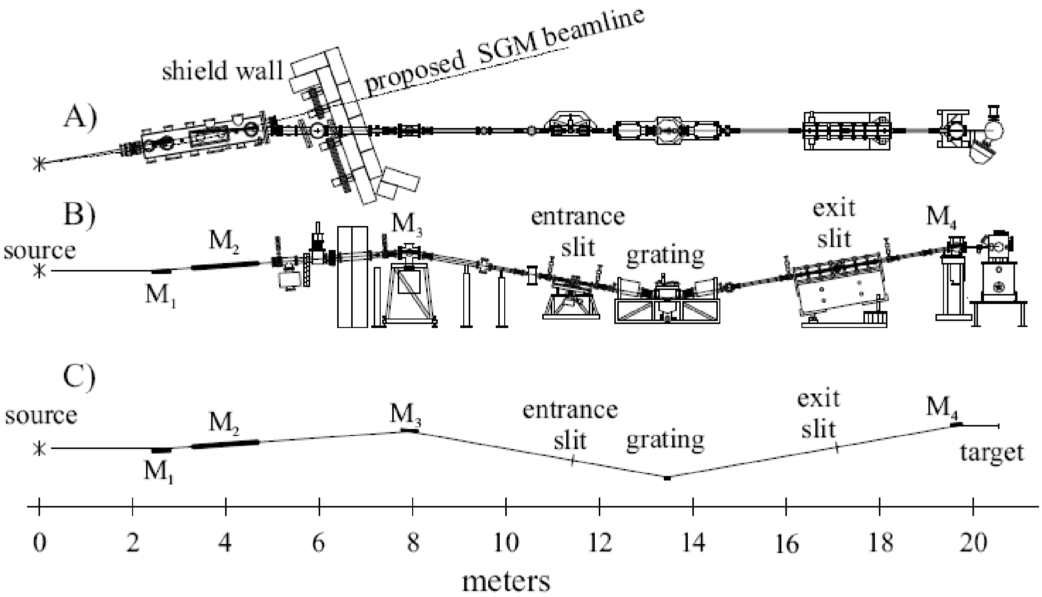

Fig 2.12 Shown above are A) top and B) side view sketches and C) side view schematic of the 6-meter toroidal grating monochromator beamline at CAMD [114]

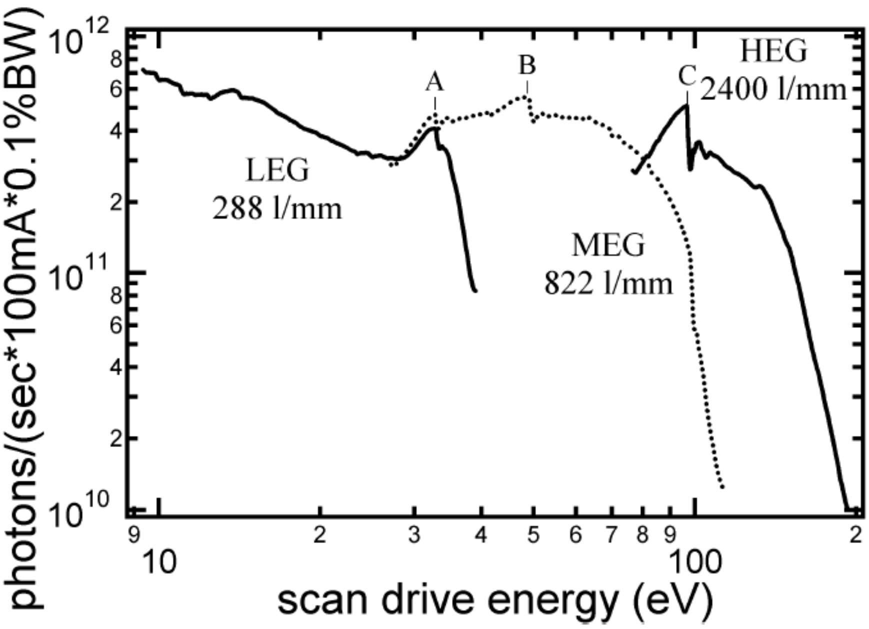

Fig 2.13 Photon flux for the 6m-TGM. [114]

In order to take maximum advantage of the intrinsic brightness of the synchrotron-radiation source, undulators are often used in a synchrotron radiation facility. A common undulator is an array of closely spaced vertically oriented dipole magnets of alternating polarity. When electrons pass through this array, the magnetic fields will force the electrons to oscillate back and forth and produce radiation with higher coherency and intensity. Although an undulator is pretty long (several meters) and heavy, it has to be built to extreme precision with tolerance of just about 50μm. A Wigglers is similar to an undulator but usually has higher fields and fewer dipoles, so they can produce a broader spectrum with a higher intensity. Fig 2.14 shows a schematic drawing of an andulator.

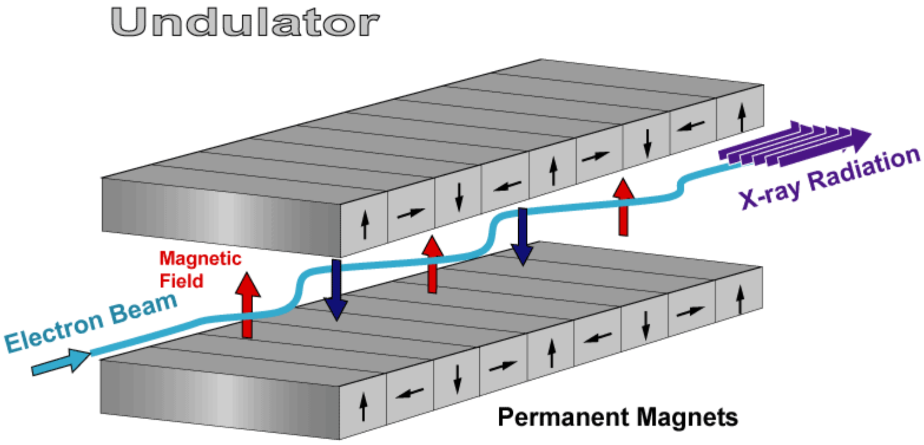

Fig 2.14 A schematic drawing for an undulator. [117]

The fourth-generation synchrotron radiation is currently being built and will become operational next year. The radiation is based on the free-electron laser concept. The X-ray laser will produce ultrashort X-ray pulses and enable people to study materials with much greater detail and much shorter time scale. As a result, many reactions that's too fast to be investigated by today's synchrotron radiation will be possible in the near future.

2.7 Experimental setup

Experiments were done at both the lab on UT campus and synchrotron radiation facility at CAMD. The UHV chamber on campus has a VSW HA150 analyzer , a Helium discharge lamp, an Auger system with a CMA analyzer, a Varian LEED system, an EELS system, a UTI mass spectrometer, a sputtering gun and a MBE evaporator. A 400l/s ion pump and a Titanium Sublimation Pumping (TSP) with liquid nitrogen cooling guarantee extremely high vacuum to 10^{-11} Torr. Fig 2.14 shows the UHV chamber for photoemission experiment at the UT lab.

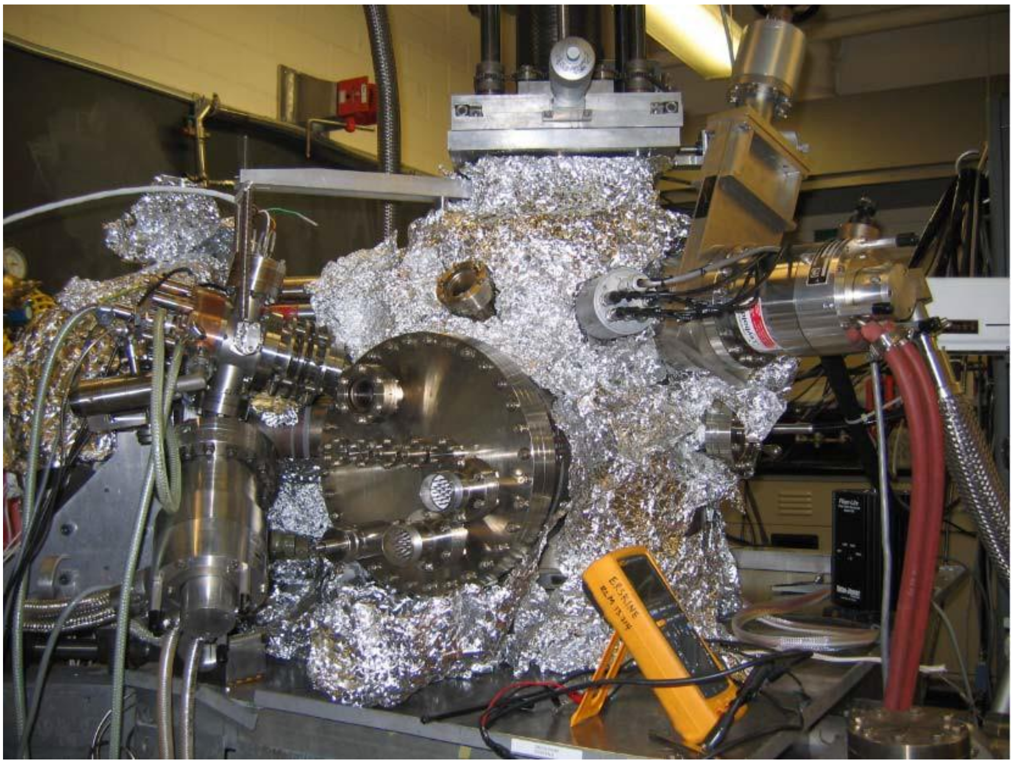

Fig 2.14 The UHV chamber for photoemission experiment at the UT lab.

The UT-Austin endstation at 6m TGM beamline at CAMD has a the same VSW HA150 analyzer, a rear-view Omicron LEED, a VSW HA30 analyzer inside the chamber for angle resolved spectra measurement, an Auger system with a hemispherical analyzer, a sputtering gun for sample cleaning. The major difference from the chamber on campus is it has bigger ion pump and TSP. So the pumping speed is faster than the chamber on campus. Fig 2.15 shows the UT endstation at CAMD.

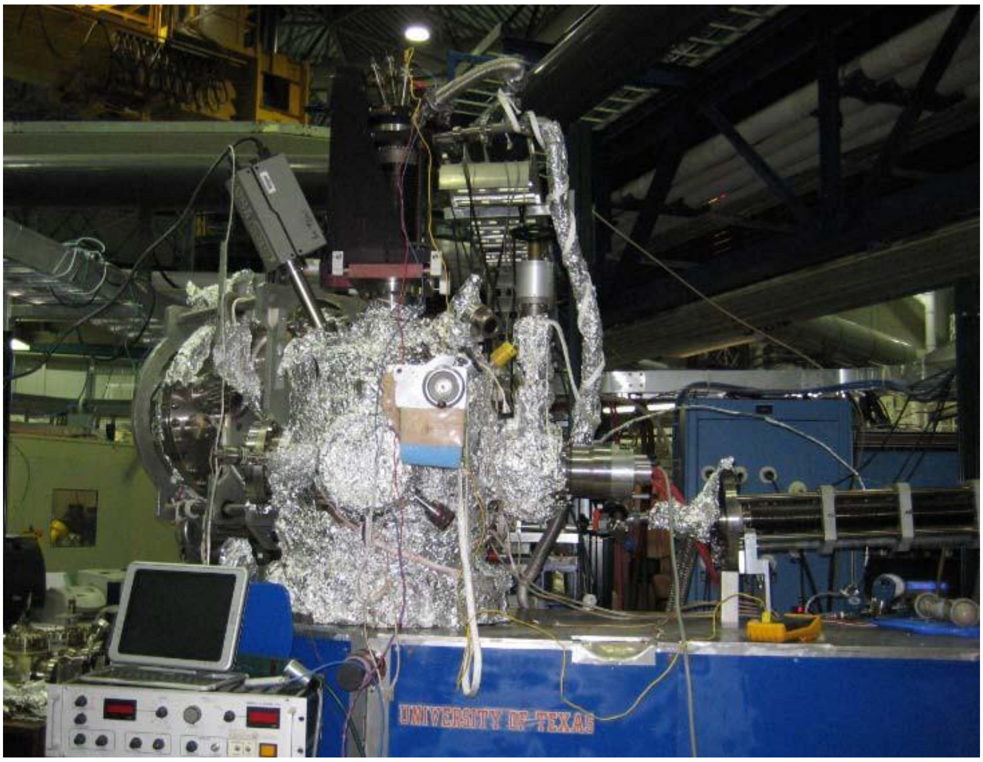

Fig 2.15 UT-Austin endstation at the 6m TGM beamline in Baton Rouge.

2.7 Sample making and ex-situ preparation

Most of samples for the experiments are made by ourselves. Single crystal boules can be purchased from a few companies like Goodfellows. The boules are grown with its axis along a specific crystal direction. We first need to find the right surface ,for example (110) surface. We align the sample on a holder so that the right surface can be cut. Our

X-ray Laue machine can give us information for the crystal alignment. After we get approximately right alignment, we use an Electric Discharge Milling (EDM) machine to cut the crystal. Our EDM machine uses a moving-wire electrode to cut crystals. A special dielectric EDM fluid is used to conduct electricity when it breaks down between the electrode which carries high voltage and the sample which is grounded. The EDM machine can cut any metal crystal with a minimum of surface damage. There are a few knobs on the EDM machine which let you choose different settings like gap, output power etc. Those settings will finally determine the cutting time. Usually the more time you spend , the more smooth cut you get. It also depends on crystal materials. Some crystals (like tungsten) can take much longer time to cut than others (like copper)

After cutting , the surface we get is quite rough. We have to go through a series of mechanical polishing to make it as smooth as possible. First we need to mount the crystal on a stainless steel polishing jig. The polishing jig allows the sample to be adjusted within 0.5^o of any desired orientation based. In order to get a Laue picture from the sample, we need at least a fine polishing until the sample obtains a mirror-like surface. . After that we can use the X-ray machine to verify if the surface is aligned correctly. A Laue camera installed on the X-ray machine allows diffracted x-ray exposed on a high speed Polaroid film. The diffraction pattern can easily tell you the crystallity[89, 90] For this we need to compare the Laue picture with patterns computed by a computer software like OrientExpress[91]. If we find there are certain degrees off, we have to use laser to align the sample on a sample mount so that the surface we need is perpendicular to the axis of the mount. Then we go to the rough or fine polishing again to acquire the right surface. The alignment and polishing cycle can repeat several times to guarantee the surface is right. When handling a single crystal, great care must be taken to avoid big impacts on the crystal, otherwise it may lose its single crystallinity. For each step of polishing, we can use a magnifier or Atomic Force Microscope (AFM) to check the quality of the surface. The grit size is reduced only when all of the scratches on the sample appears uniform in depth. The rough polishing uses sand paper with grit sizes 300, 600, 800. After the rough polishing , the surface is relatively smooth. Then fine polishing with polishing powders of alumina ranging from 0.06 microns to 25 microns. Nylon polishing pads are used instead of sand paper during the fine polishing. When the polishing goes down to 1 micron, a felt pad is needed to get shinier surface. Great care needs to be taken to make sure the debris is cleaned before a smaller size power is used. Some samples need electrochemical polishing after the mechanical polishing

The EDM machine can also drill holes on the sample. It can drill a hole as small as 5 mil without any physical strain on the sample. For detailed polishing procedures , you can go to David Lacina’s master thesis [92]

Fig 2.16 An Electric Discharge Machine (EDM) used for cutting a sample off a single crystal boule and machining mounting holes into a crystal. On its right side is the X-ray machine.

Sample holder design

In order to clean the sample effectively, get the sample cool down to desired temperature and adjust the position of the sample easily, a good sample holder design is prerequisite. For this I designed a sample holder that can effectively heat the tungsten sample and at the same time rotate the sample in two degree of freedom for large angles (more than 180 degrees). There are many other designs that I made like evaporators with several sources, improvement of the helium cold stage etc. I will not write those things in details in this thesis.

Chapter 3

Photoemission study on stepped W(110) surfaces

3.1 Core level photoemission study on stepped W(110) surface

Steps on a high index metal or semiconductor surface may play a fundamental role for electronic structure, adsorption, film growth, chemical reaction, catalysis. There are different atoms on the stepped surface associated with different coordination numbers. Atoms on step edge usually have smaller coordination number compared with terrace atoms. Thus electronic properties around step edge can be quite different from the flat part of the surface. Surface core level shift studies on single crystal have been done extensively during the past 20 years. [122,123] But most of those studies can only distinguish between surface peak and bulk peak. There are also many research efforts on molecules absorbed on stepped surface. They are trying to get electronic information around the step edge. However, in this case the information is gained via the adsorbate rather than the substrate yielding different but complementary information. Due to surface relaxation and reconstruction , step edge atoms might be quite different from the behavior expected from coordination numbers. There have been several studies on W(320) surface , but so far no conclusion has been made due to poor experiment conditions. On early studies[129][130], it was shown that the step edge atoms have a large SCLS than the W(110) . So they claimed the coordination number relationship exist for this system. However later on another research group showed a quite different result[125].They found that the surface peaks in the W(320) spectra become closer to the bulk binding energy compared with the case of the W(110) spectra. And the component from the step edge atoms was believed to fill the valley between the bulk and surface peaks in the flat W(110) spectra. They found their data didn’t agree with tight binding calculation which assumed no surface relaxation and reconstruction on the W(320) surface. They also performed nonlinear least squares analysis with a variety of model functions and found that the average SCLS for W(320) is only about 140 meV which implies the absence of a large SCLS for the step-edge atom. In order to explain Riffe et.al.’s data, Cho et al [127] did ab initio calculation including both initial and final effects for the W $4f_{7/2}$ surface core level shift at W(320) surface. They concluded that core hole screening effect may cause the smaller SCLS for W(320) atoms. Their calculation shows a core hole on the W(320) stepped surface is less screened than the core hole in a bulk atom while the screening of a core hole is enhanced on the flat W(110) surface. However, both their initial state and final state theory calculations predict largest SCLS for the step-edge atom. This is consistent with our experiment and contrary to Riffe’s.

In this study for the first time we show a distinctive component from step edge atom on the vicinal tungsten surface. And we still conclude that the surface coordination plays a fundamental role on the surface core level shift, thus the surface core level shift has the potential to distinguish different types of atoms on a step surface.

We have measured three samples with different vicinal angles, namely W(110), W(320), W(540). W(320) surface was cut 11.3 degree off from (110)surface and W(540) surface was cut 6.3 degrees from (110) surface. For the W(320) surface, the steps are separated by five atom wide (110) terraces. Figure 3.1 shows the drawings for stepped W(320) and W(540) surfaces. On W(320) we labeled 6 different rows of surface atoms. Atom 1 is the step edge atom and has smallest coordination. Atom2 to 4 are terrace atoms. Atom 5 is base atom and Atom 6 is the corner atom that lies under the row of atom 1. W(540) surface has a similar structure but with 9 atoms terrace width.

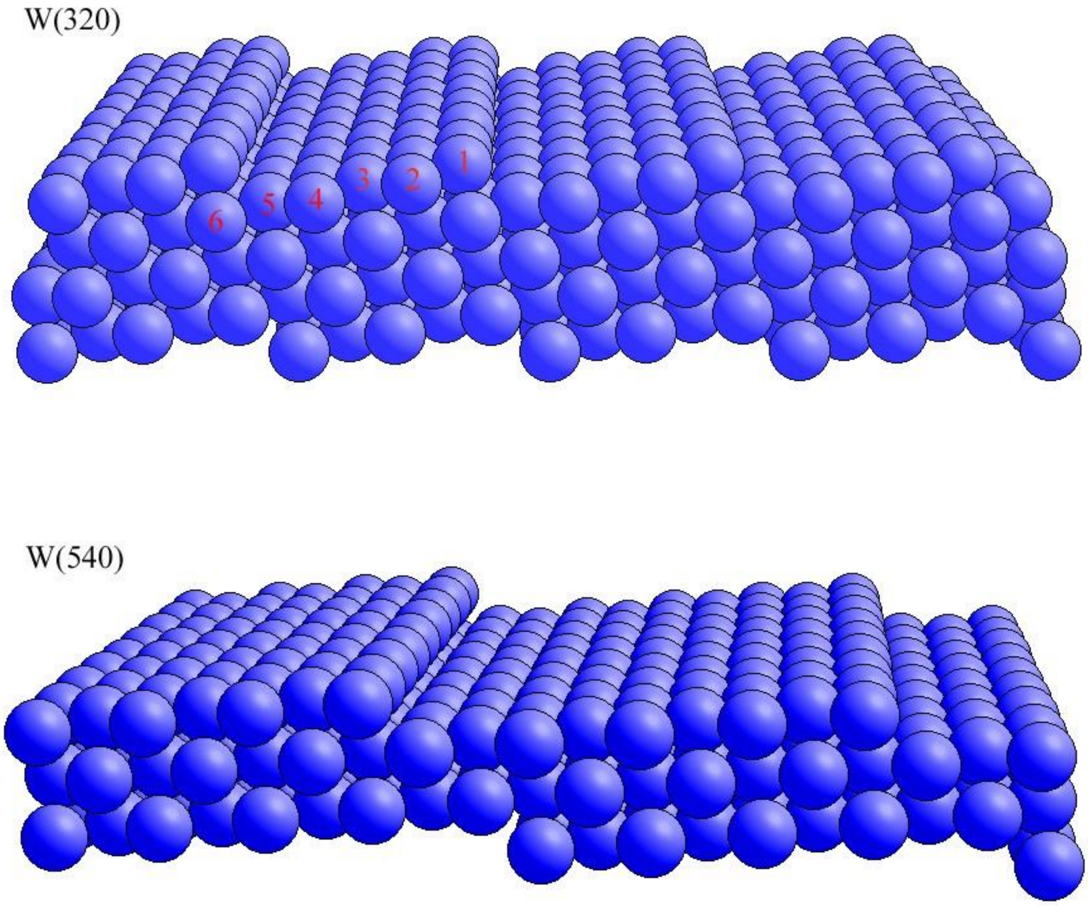

Fig 3.1 Drawings for W(320) and W(540) stepped surfaces. Different rows of atoms 1 through 6 are labeled on W(320) drawing.

The experiment was done at UT-Austin 6meter TGM beamline at Center for Advanced Microstructures and Devices (CAMD). The base pressure was 1x10^{-10} Torr. The sample was cleaned by repeated cycles of annealing in oxygen at 10^{-8} Torr followed by rapid flashing in UHV for a few seconds. The cleanness of the sample was checked by

LEED and tungsten 4f core level peaks. For W(320) and W(540) we see clear splitting spots indicating high quality stepped surfaces. Photon energy of 70eV was chosen to maximize the surface peak. The photon is incident on the sample with 45 degrees. Photoelectron spectra with different emission angles are measured. Figure 2 shows the measured spectra for 3 different surfaces. The emission angle is normal to the (110) microsurface for each case. The spectra from all the three surfaces show a very strong peak for the surface component. This is substantially different from all previous experiments which only show a broad spread of the surface component. For curve-fitting, we use Doniach-Sunjic lines [86]convoluted with a Gaussian broadening. For W(320) and W(540) surfaces, the curve-fitting can be done with 4 or 5 components (peaks). Four components are enough to get reasonable results. For surface components, the life-time width and singularity index were constrained to the W(110) surface-atom values (80meV and 0.063, respectively). For bulk components, the life-time width and singularity index were fixed to 65meV and 0.035 respectively. Those values are obtained from previous experiments [122][125]. The Gaussian width is about 100 meV for both surface and bulk components through curve-fitting this time.

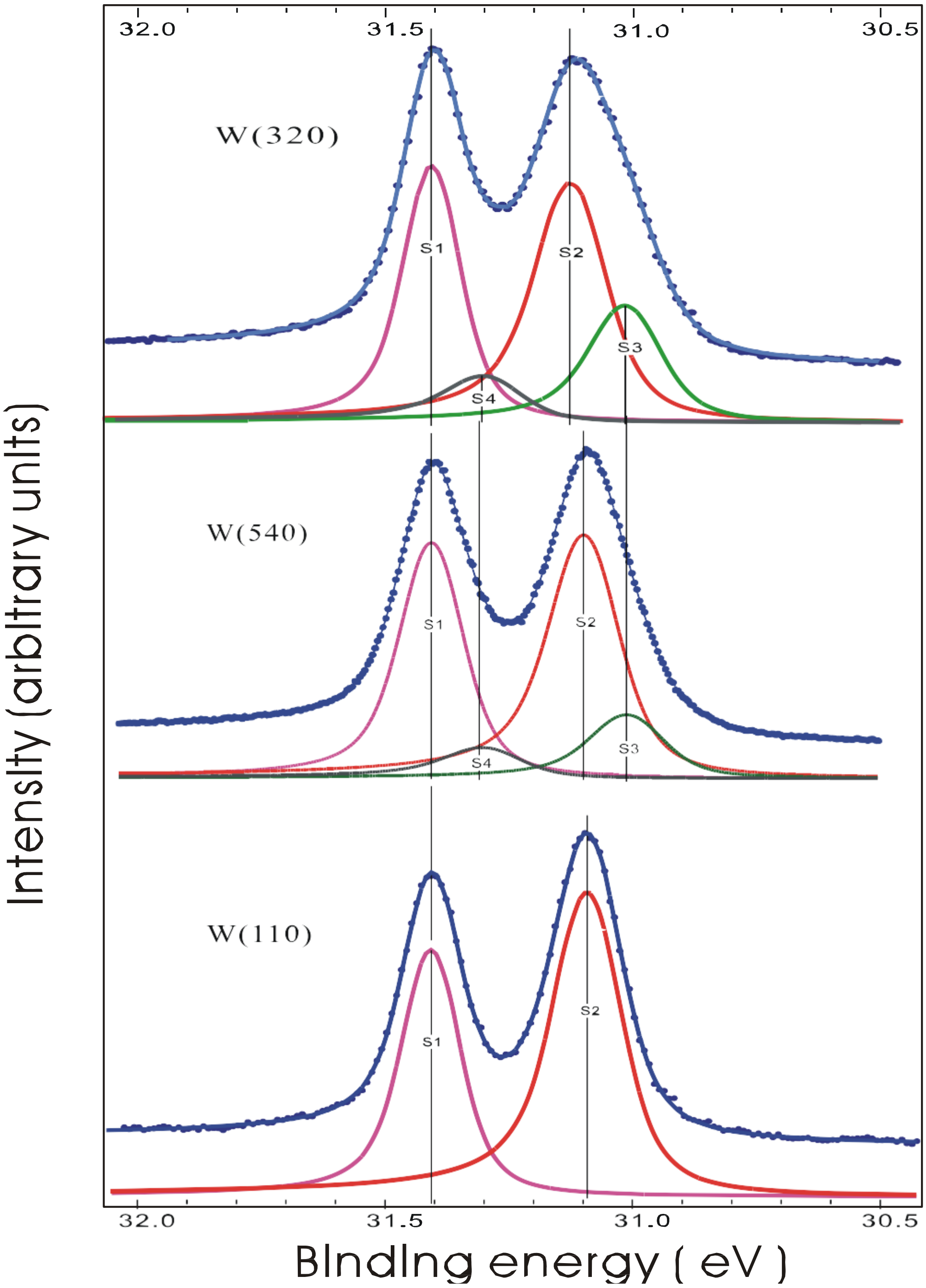

Fig 3.2 W 4f $_{7/2}$Core level Spectra from 3 different tungsten vicinal and flat surfaces

For W(320) peak 2 has SCLS 0.283 eV, its intensity is stronger than other surface peaks. Thus, it should be attributed to the terrace atoms on the stepped surface. Peak 2 from W(540) has SCLS 0.304eV, which is a little smaller than the surface peak for W(110) (0.318eV). For peak 3, the SCLS for W(320) and W(540) are both 0.380eV. This should come from the step-edge atoms which have smallest coordination numbers. The peak 3 from W(320) is strong enough to contribute a shoulder to the whole surface peak. Its integrated intensity is above one half of the peak 2. This is higher than we expected for the step-edge atoms, which only has one row compared to 3 or 4 rows on the terrace. The peak 3 from W (540) has integrated intensity ¼ of the peak 2, which seems to be reasonable. The strong peak 3 from W(320) could be caused by photoelectron diffraction.

Previous experiments only got a very broad surface peak. Under Riffe at al's study[Fig 3.3], SCLS from the terrace peak (S1) can change from 270meV to 315meV depending on different fitting methods. On average it gives a SCLS of about 290meV, very close to our results for terrace atoms from both clean and hydrogen contaminated surfaces. However, for the SCLS from the step-edge atoms(peak 2), they got a much smaller value (about 180meV) than ours. For the large observed spread in surface spectrum weight, Riffe et al. assumed a global reconstruction where all the atoms are similarly displaced agrees on average with atomic coordination estimate.

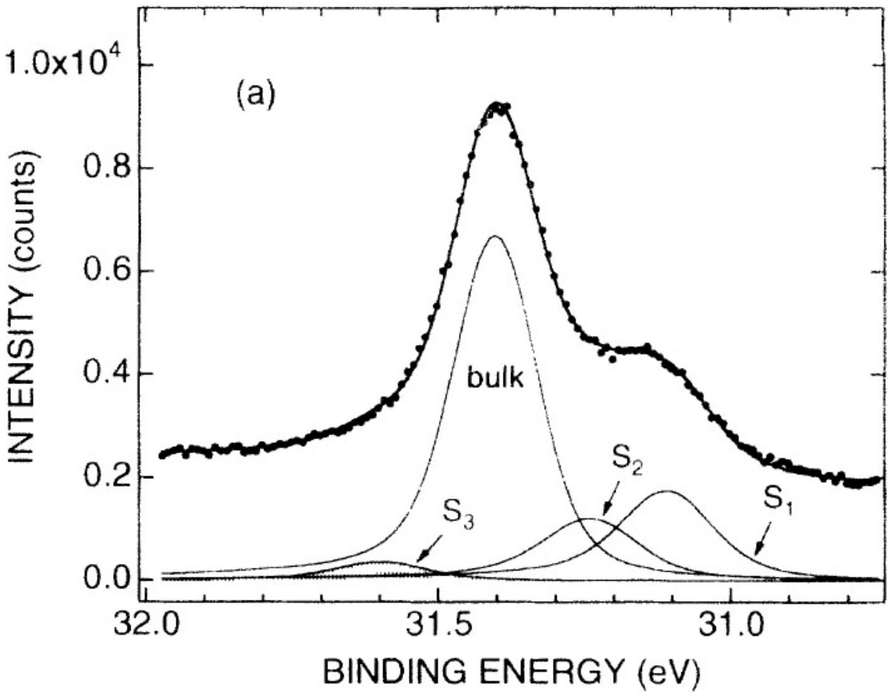

Fig 3.3 W 4f $_{7/2}$ Core level spectrum adapted from prior experiment [125]

For reference [129] and [130], although they claimed large SCLS for the step edge atoms, the whole surface component is also spreading and no obvious peak can be found. Also, their binding energy calibration might have some flaw. Based on Riffe's analysis, reference [129] and [130] would have the similar result with Riffe if the system error is corrected.

Ref [125] also suggests that Smoluchowski effect may play a role for the broadening of the surface core level peak. Smoluchowski is the first one to propose the concept of charge smoothing. [121] He assumed for a stepped surface, electrons move from the step edge toward the lower terrace in order to lower their potential energy. The redistribution of electrons will generate a force that makes the atoms near steps undergo structural relaxations. This relaxation will modify the electronic structure at the stepped surface, causing a wave function change around the steps. Thus the core level binding energy for the atoms near the steps will be changed through the Coulomb interaction between the core and valence electrons.

The atoms near steps undergo structural relaxations, due to the new forces generated by the redistribution of the electrons. These modifications of the electronic and structural properties at the stepped surface are expected to affect the core-level binding energy of the atoms near steps, influenced by the change in local valence charge density via the Coulombic interaction between the core and valence electrons.[126] In our spectrum, we do find the effect of this kind of structural relaxation. We find that the surface peak from the terrace atoms has a apparent shift (about 30 meV) toward higher binding energy for W(320). For W(540) a smaller shift is found compared to W(320). This difference can be explained by the smaller step density of W(540). However, this surface relaxation is much smaller than Riffe’s conclusion. Table 3.1 shows the SCLS for step edge atoms of W(320) from different research groups.

Table 3.1 SCLS for step edge atoms of W(320) from different research groups. The binding energy unit is meV

This work	Tight binding calculation[125]	Cho et at[126]	Riffe et al[125]	Purcell et al[129]	Chaveau et al[130]
380	390	230	190	420	590

We also compared our data with the *ab initio* calculation from Reference [127]. The calculation obviously could not fit either our data or Riffe's data. They claimed the final state effect (core hole screening) may play an important role. They said the core hole screening has opposite effect on the W(110) and W(320) surfaces. To be specific, the core holes in (110) terrace of W(320) are found to be less screened than those in bulk atoms, leading to a decrease of the SCLS. We could not see this effect from our data. The ab initio calculation also finds the SCLS from the step-edge atom is larger than the SCLS from those terrace atoms. This agrees with our experiment and is contrary to Riffe's paper.

While our result is quite different from the previous experiments, it agrees with tight binding calculation very well. Fig 3.4. shows the tight binding calculation from reference [125][130]. The major similarity of this calculation with our experiment is very close value of SCLS for the step-edge atoms (390meV for the calculation). The binding energy for the terrace atoms (287meV) also agrees with our experiment. The major difference is that the intensity from step-edge atom is smaller than our experiment. We compared this calculation with the measured W(320) core level spectra with 15 degree emission angle. (Fig 3.5) Great similarity is found between the two spectra. From figure 3.6, we can see that the step-edge peak is much smaller than normal emission. Thus the intensity of step edge peak is considerably affected by emission geometry. This could be caused by photoelectron diffraction effect.

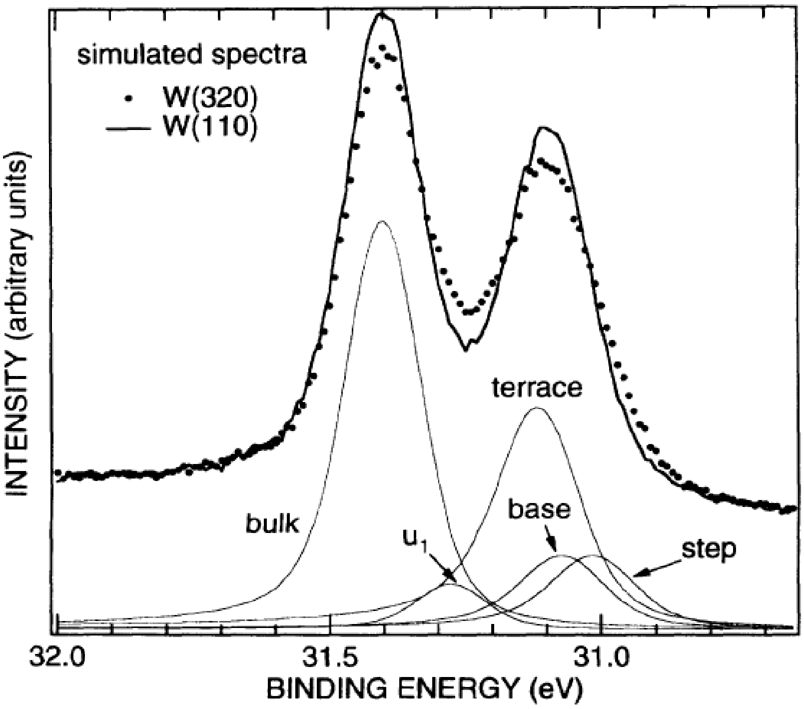

Fig 3.4. Tight binding calculation for W(320) and W(110) surface from reference [125]

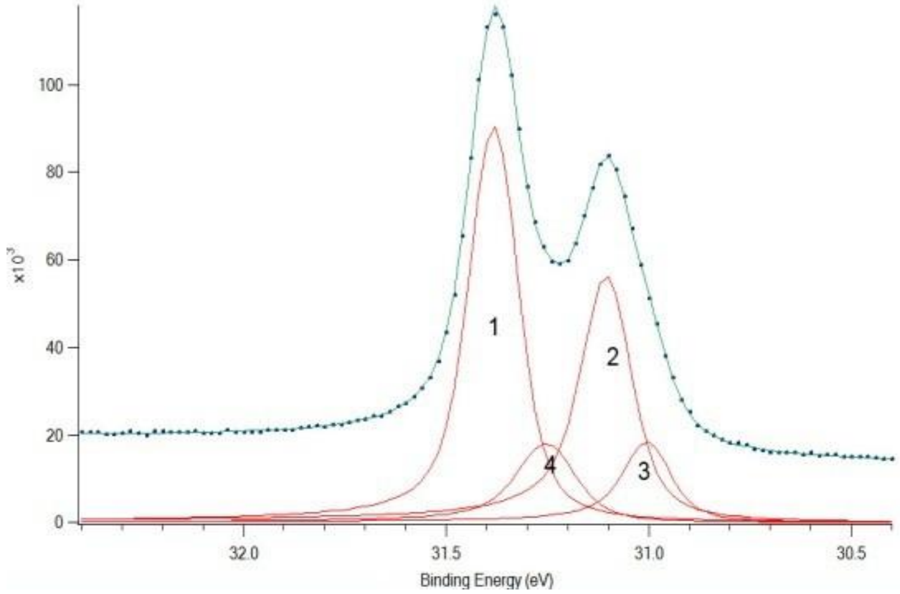

Fig 3.5, W(320) 4f core level spectrum measured with 15 degree emission angle

We compared our work with prior experiments and calculations on several different types of tungsten surfaces, namely W(100), W(110), W(111), W(320). The W(111) experimental data are from Ref [123], the W(100) data are from Ref [128] , W(110) experimental data are from Ref [131] and W(320) calculations are from Ref[127]. The W(320) data are from the current study. We find that if we consider atom neighbors up to the third nearest neighbors and calculate the coordination parameter C as

$$C = \sum_{j=1}^{3} n_j / r_j$$

Where n_1 represents number of nearest neighbors, n_2 is the number of second nearest neighbors, n_3 is the number of third nearest neighbors. r_j is the corresponding distance between the surface atom and its neighbor in the unit of lattice constant. Table 3.2 shows the coordination parameters and the corresponding surface core level shift from prior experiments and calculations and also the current work.

Table 3.2 Coordination numbers and surface core level shifts for several different tungsten surfaces. nn means the number of nearest neighbors, nnn means the number of second nearest neighbors and nnnn means the number of third nearest neighbors.

Tungsten surface	**SCLS(meV)**	**nn**	**nnn**	**nnnn**	**C**
W(100) surface	360	4	5	6	13.86
W(100) subsurface	91	8	5	8	19.90
W(111) surface	430	4	3	5	11.16
W(111) subsurface	110	7	6	9	20.45
W(110) surface	321	6	4	7	15.88
W(320) step edge	380	4	4	4	11.45
W(320) terrace*	280	6	4	7	15.88
W(320) base/corner$^{\Delta}$	108	8	5	9	20.60
W(540) terrace*	280	6	4	7	15.88
Bulk	reference	8	6	12	23.72

* atom 2 has 6 third nearest neighbors.

$^{\Delta}$ base atom has 6 nearest neighbors

Figure 3.6 shows plot of the surface core level shift versus coordination parameter C. We use several columns with different heights to represent the theoretical calculations which have a broad range of calculated values. The height of the column is proportional to the range. We can see that most of the data fall on or close to a linear trendline, i.e., the surface core level shift increases almost linearly with decrease of the coordination parameter. This demonstrate the rightness of the coordination number theory. Only the W(320) data by Chaveau et al. is far off the line. That could be caused by systematic error.

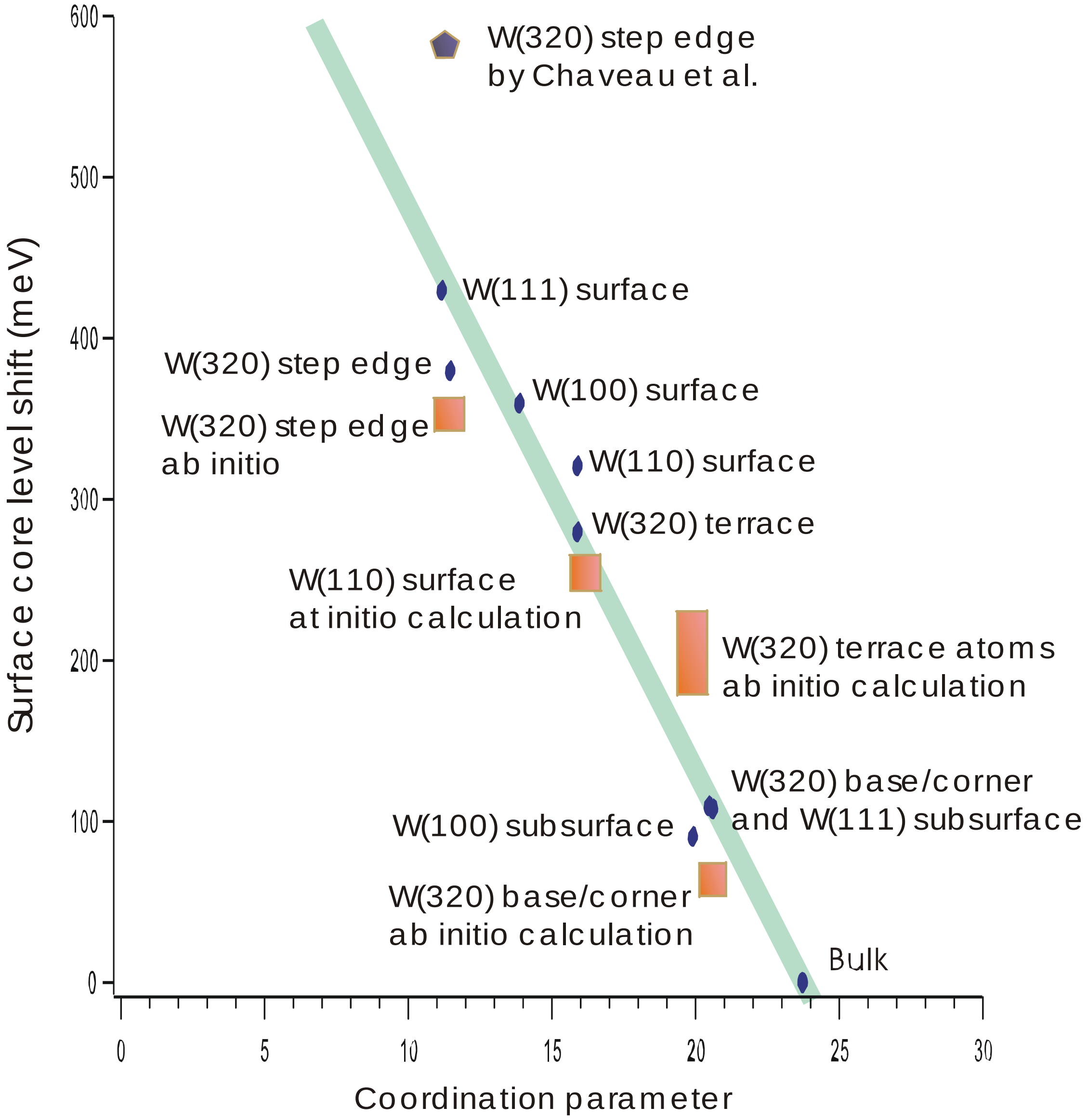

Fig 3.6 Surface core level shifts vs coordination parameter for several different tungsten surfaces. The orange columns are theoretical calculations and the column height represents the broad range for the calculated result.

For the prior experiments[125,130], from the shapes and the smaller SCLS , we think the surface might be contaminated by Hydrogen. For a hydrogen molecule , it has to break down into two hydrogen atoms in order to have stable chemical bond with tungsten atoms on the surface. A step edge atom has fewest nearest neighbor compared with a bulk atom, thus it could be more likely to attract hydrogen. The whole stepped surface can be viewed as a surface with large density of defects. These defects would catalyse the breakdown of H_2 thus promote the hydrogen bonding. As a result , the vicinal W(110) surface will be easier for hydrogen to stick on than the flat W(110). Thus we checked our core level spectra for W(320) surface with a little dose of Hydrogen (3.5L). The geometry is same as Fig 3.2. Fig 3.7 shows the experiment result. Through curve fitting procedure described above, we got four components for the W $4f_{7/2}$ spectra. We can see the step edge peak is completely gone. We constrain the bulk peak with same shape and life-time width as clean surface. For surface peaks, the singularity index and life-time width are released because the tungsten surface atoms can be chemically and structurally modified by hydrogen. [124, 131] The Gaussian width from the curve-fitting is a little broader than the clean counterparts(about 160meV on average). From the decomposed curves we can see that the S1 component has a binding energy of 272 meV, a little smaller than the terrace atoms component for the clean stepped surface. But the shift is much smaller than the surface peak shift for the hydrogen dosed W(110) on Ref [131] for the same amount of dosing. So we believe the S1 component is still the terrace component for the clean surface with just a little affected by hydrogen. By comparing to the bulk peak, we found that the intensity of terrace peak decrease by about 1/2. A new peak (S2) appears between the bulk and terrace peak with SCLS of 160meV. This could be caused by modification of coordination by hydrogen atoms stick on the step edge. The similar intensity as the step edge peak for the clean surface further confirms this assumption. The peak S3 has a binding energy larger than the bulk. This looks unphysical but it is consistent with the S3 peak in Fig 3.3. The broadening shape of the surface peak looks similar to previous experiments[125, 129, 130]. The only difference is the terrace component has a little smaller SCLS. The temperature control or defect density may cause the difference.

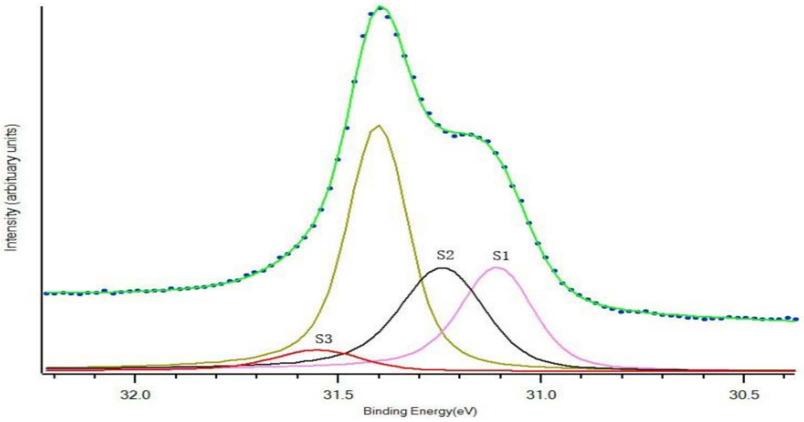

Fig 3.7. Core level spectrum of W(320) with Hydrogen dose of 3.5L

In conclusion, we measured the surface core level shifts for different vicinal W(110) surface and find that the step edge peak has the largest binding energy. This is contrary to the previous experiments but consistent with theoretical calculations. The SCLS from the stepped surfaces can distinguish different types of atoms with different coordinations. The hydrogen dosed experiment on the stepped surface further confirms the step edge atoms are easy to attract hydrogen atoms and thus the stepped tungsten surface is easy to be contaminated compared with flat tungsten surface.

3.2 Ag nanowires growth on stepped W(110) surface

Although stepped tungsten surface can be a good candidate to serve as substrate for self assembly nanowire growth, very few experiments have been found so far. We grew Ag on the stepped W(110) surfaces and used Angle Resolved Photoemission to study the band dispersion along the step and perpendicular to the step. Photon energy is 70eV The coverage is 2ML. Fig 3.8 show the angle resolved spectra taken along the steps. Fig 3.9 shows the spectra taken perpendicular to the steps. The strong dispersion along the steps and little dispersion perpendicular to the steps indicate one dimensional character(wires) along the steps.

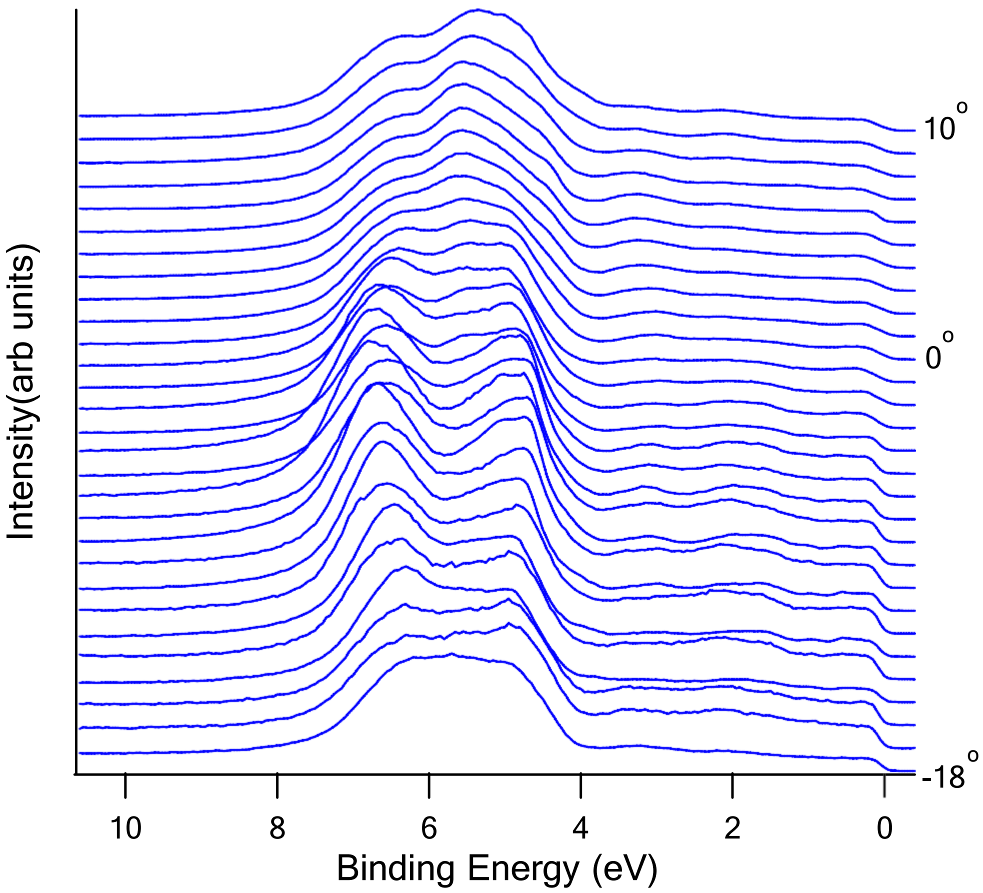

Fig 3.8 Angle Resolved Photoemission spectra taken along the steps for Ag growth on W(540). The photon energy is 70 eV.

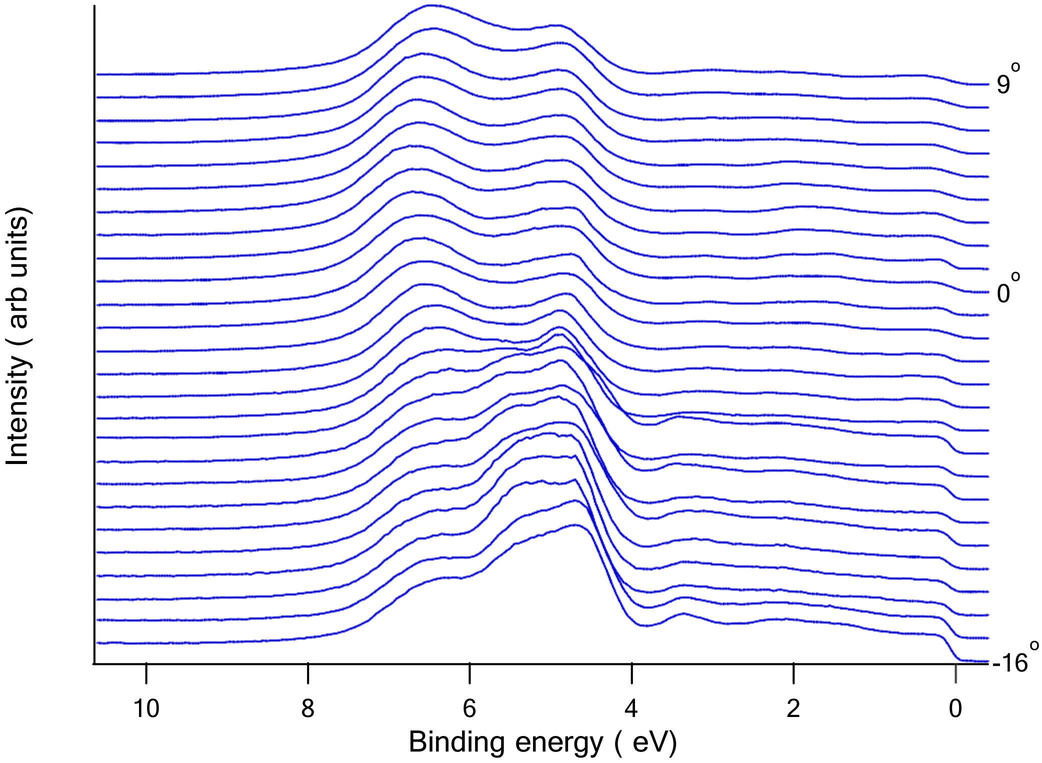

Fig 3.9. Angle Resolved Photoemission spectra taken perpendicular to the steps for Ag growth on W(540). The photon energy is 70 eV.

Chapter 4

Core level photoemission study of Cesium on Cu(100)*

The adsorption of alkali metals on solid surfaces has been studied for many years. One reason is because alkali atoms have a single ns valence electron thus provide one of the simplest models for theories of chemisorptions on metal surfaces.[101] A more important drive for the extensive studies is because of the technological applications that makes use the ability of alkali adatoms to change the electronic and chemical properties of surfaces. There are many important discoveries during the past 20 years for alkali on solid. For example , the observation of condensation of the alkali adatoms into dense 2D phases at relatively low coverages [104] The charge transfer from alkali adsorbates to graphite surface(HOPG) leads to band filling and surprising gap opening in the surface electronic structure of graphite[102] and the substantial activity of adsorbed alkali in catalysis [103] Despite being one of the earliest chemisorptions systems to be studied, finding the answer for the charge transfer and polarization or depolarization is a difficult job. It is not easy to measure spectroscopically the degree to which the chemisorption bond can be described as ionic or covalent . Langmuir and Gumey did pioneering work that describe the formation of electrical double layers for electron transfer from alkali metal to the substrate.[132,133]

However, it is not clear whether this charge is completely localized on the substrate ionic stated, or if an occupancy of the *s*-derived state is still present spartially ionic state with some covalent charactered.

- Data Part of work by K Koch

4.1 Phonon broadening study of Cs $5p_{3/2}$ core level spectra

When atoms in a solid vibrate the charge cloud is deformed and the localized core electrons find themselves riding in a changing Coulomb potential. This changing Coulomb potential can cause a broadening of core-level excitation line shapes in solids. In other words, the optical excitation of a core hole is coupled to vibrational modes of the lattice. This broadening could be caused by the change of the distance between the excited atom and its neighboring atoms or by the change of force constant between the atoms. In a solid with a large number of atoms, there are very many vibrational modes. When the excited core hole state is coupled with so many vibrational modes, the resulting phonon broadening will be close to a Guaussian function. This Guaussian distribution is dependent on temperature because the lattice vibration is related to temperature. For the phonon broadening calculation in a metal, Overhauser did the pioneering work with linear coupling assumption. He used deformation-potential theory and derived a temperature dependent phonon broadening equation as Eq 4.1

$$G_{ph}^2(T) = G_{ph}^2(0)\ 1 + 8\left(\frac{T}{\theta_D}\right)^4 \int_0^{\theta_D} \frac{x^3}{e^x - 1}\,dx \qquad (4.1)$$

where $G_{ph}(T)$ is the phonon broadening, T is the temperature, $G_{ph}(0)$ is the phonon broadening at zero temperature and θ_D is the Debye temperature of the metal. $G^2_{ph}(T)$ is thus proportional to T for $T > \theta_D$. Although this work was not published, many researcher cited his formula and made related calculation and experimental curve-fitting. One of them are Hedin et al and he explained the process of phonon broadening with a pseudopotential theory.[106] Compared to other theoretical studies of temperature dependent phonon broadening by Bergersen et al[107] and Almbladh et al[108], the pseudopotential theory fit experiments very well. The main points of the theory are as following. In a metal, we treat it as a periodic positive ion lattice immersed in a free electron sea. For a specific ion ‘i’, due to all other ions vibrate relatively to it, there will be a net potential change on this ion ΔV because of the changing Coulomb potential. We can sum the induced Coulomb potential from all other ions. Since all other ions have a distance from ion ‘i’ longer than the core radius, we can use the screened pseudopotential *w* as approximation for the ion ‘j’ , then we can have

$$\Delta V = \sum_j \quad - \ _j \ - \ (\ ^0 - \ ^0_j)] \qquad (4.2)$$

Since the lattice vibrations are of small amplitude, we assume a linear response of the fluctuating potential with respect to ion position. If the core electron wave function is $u_c(\ )$, the induced potential can be written as

$$\Delta V = -f|u_c(\ )|^2 \sum_j \quad + \ - \ _j \ - \quad ^0 + \ - \ ^0_j \ d \qquad (4.3)$$

The width of the phonon distribution will be

$$\Delta^2 = < (\Delta V)^2 >_T \qquad (4.4)$$

If we use a Thomas-Fermi-screened Coulomb potential for *w* and integrate over a Debye sphere rather than over the Brillouin zone, we can calculate the phonon broadening and get the result:

$$\Delta^2 \ \frac{E_F^2 k_B \theta_D}{6u^2 p \Omega_0} \ 1 + 8\left(\frac{T}{\theta_D}\right)^4 \int_0^{8_D/T} \frac{x^3 dx}{e^x - 1} \qquad (4.5)$$

Where $hk_D u = k_B\theta_D$, u is the longitudinal sound velocity, k_D is the Debye momentum, ρ is the mass density and θ_D is the Debye temperature. For a Gaussian function the full width at half maximum is

$$FWHM := W = 2(2ln2)^{1/2}\Delta = 2.355\Delta \qquad (4.6)$$

This confirmed the temperature dependence of Overhauser's expression and the expression of W can be simplified by taking some approximations: Keep only the contributions from the longitudinal branches and consider only the nearest-neighbor atoms, then average over the directions of neighbor atoms. The simplified T = 0 expression for the phonon width at zero temperature can be expressed as

$$G_{ph}^{2}(0) = 2.355^{2}\frac{\Omega_0 h_2}{4rr^2 M k_B ()_D} k_D \left(\frac{z\;'(\;_0)}{3\;_0}\right)^2 \int_0^{k_D R_0} x f^2(x)dx \qquad (4.7)$$

The integral in equation is about 7.9 if we give the value of $k_D R_0$ as 4.25 for bcc metal and 4.38 for fcc metal. All the quantities in the equation can be measured by experiment except the derivative of the pseudopotential at the nearest-neighbor distance, $'(\;_0)$. Hedin et al demonstrated that $'(\;_0)$ is not sensitive to the cutoff parameter for alkali metals. Thus the phonon width can be expressed as

$$G_{ph}^{2}(0)()_D = c \qquad (4.8)$$

where C is a constant that depends upon the derivative of the nearest-neighbor screened pseudopotential and the mass density of the solid. Other theoretical studies of temperature dependent phonon broadening[107, 108] also exhibit the temperature dependence of Eq. 4.1. Later on there are some research using an analytical approximation of the integral in Eq 4.1, this can be expressed as

$$G_A^2(T) = G_{ph}^2(0)\,[1 + (\frac{8\,T}{3\,\theta_D})^2\,]^{1/2} \qquad (4.9)$$

This expression was used to analyze temperature-dependent core-level phonon broadening by several research groups[109-112] and also mentioned by Riffe et al[113] . This formula gives the same high temperature and zero temperature approximation as Overhauser's formula(Eq. 4.1), but in the medium range of temperature, it doesn't give very precise approximation. For this Riffe et al gave a better formula to replace Eq 4.9 [113], it can be written as

$$G_E^2(T) = G_{ph}^2(0)\,\coth(\frac{3}{8}\frac{\theta_D}{T}) \qquad (4.10)$$

Riffe et al. compared the difference between Eq 4.9 and Eq 4.10 (Fig 4.1). We can see that in a broad range of temperature, Eq 4.10 is much closer to Eq 4.1 than Eq 4.9.

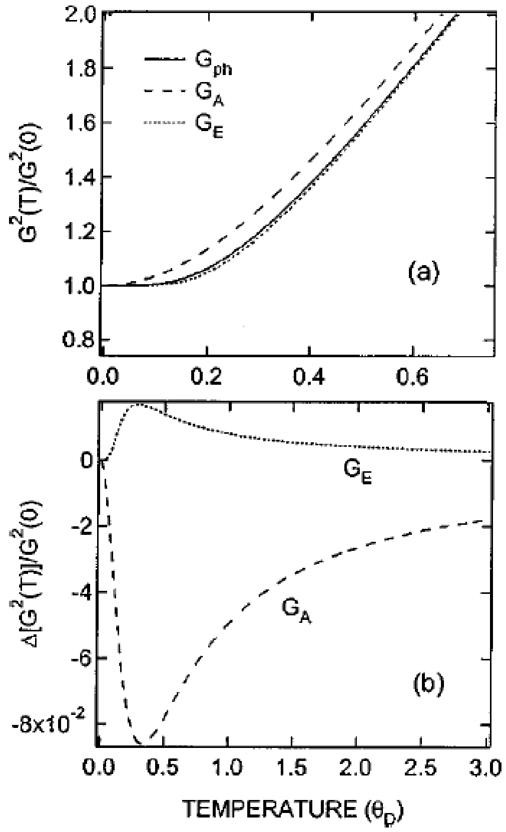

Fig.4.1 Comparison of model phonon broadening (Eq. 4.1) with analytical phonon broadening approximations G_A (Eq. 4.9) and G_E (Eq. 4.10). (a) Normalized squared Gaussian widths. (b) Differences in squared widths between Eq. 4.1 and the approximations. Adapted from [113]

If we consider the non temperature effect on the phonon broadening determined by the instrument,[114] there will be another added term to Eq 4.10

$$G_{ph}^2(T) = G_{nst}^2(0) + G_{ph}^2(0)\coth\left(\frac{3}{8}\frac{\theta_D}{T}\right) \qquad (4.11)$$

$G^2_{nst}(0)$ represents the instrumental contribution to the broadening. We can get it from analyzing the Fermi edge spectra. In our experiment, at 20 eV photon energy, for example, the instrumental resolution is measured to be 67 ± 2meV .

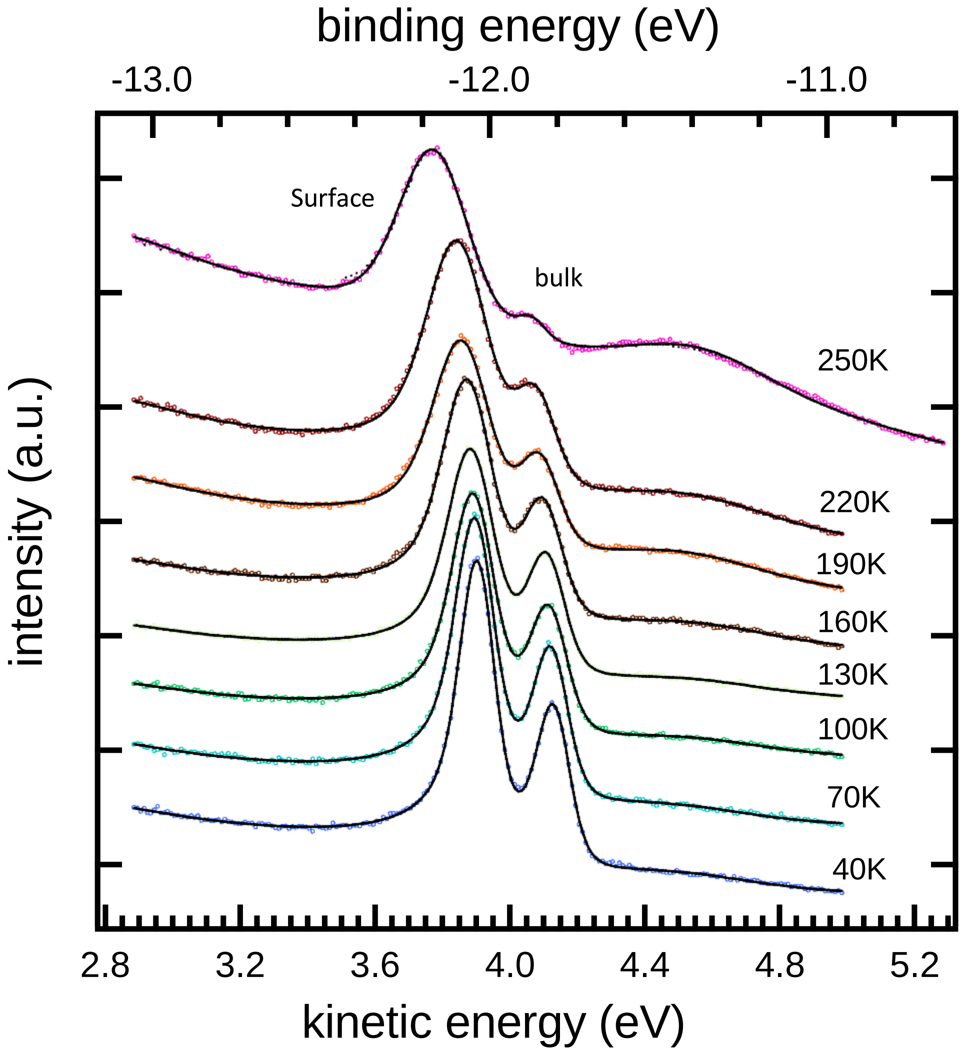

Fig 4.2 Temperature-dependence of the Cs $5p_{3/2}$ core level spectra measured at 20 eV photon energy.

Fig. 4.2 shows the temperature-dependence of the Cs $5p_{3/2}$ core-level spectra measured with 20 eV photon energy. The beamline exit slit was set to 300μm and the pass energy of the HA150 analyzer was set to 5eV. Curve-fitting to Doniach-Sunjic lineshape convoluted with Gaussian broadening was done for each single spectrum. We assume that the interface peak has a singularity index which is equal to that of the bulk, and that the singularity indices for the surface and the bulk were their 40K values. We got the Gaussian broadening G(T) for each temperature we measured through the curve-fitting.

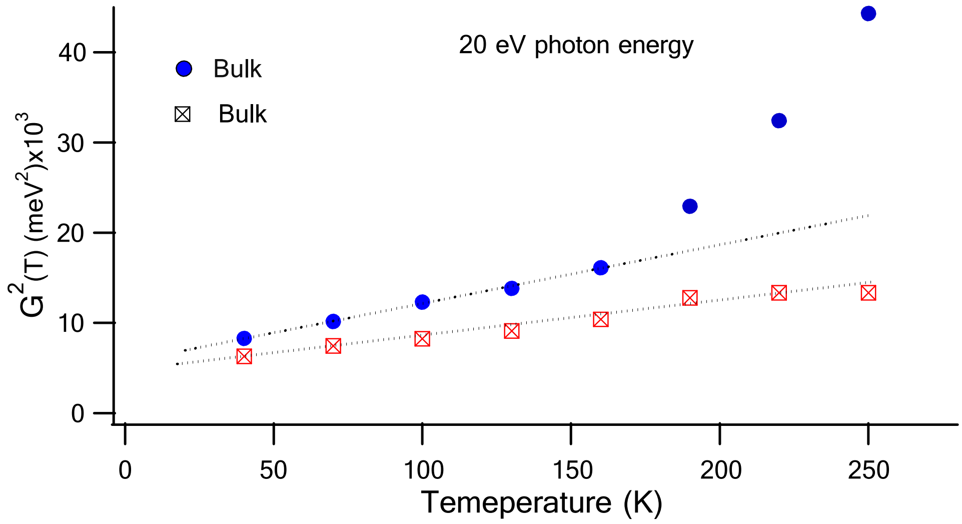

Fig 4.3 Square of Gaussian broadening vs. temperature for bulk and surface peaks. The dashed lines are the least square curve-fittings to Eq 4.11.

Fig 4.3 shows the square of Gaussian broadening as a function of temperature. From the figure we can see that the bulk and surface curves are well separated. Next the temperature dependence of the experimental Gaussian widths were least-squares analyzed using Eq. 4.11 to determine best-fit values of $G_{ph}(0)$, θ_D , and thus $c = G_{ph}^{2}(0)()_{D}$ for both surface and bulk peaks. The dashed lines are the fitted curves for Eq 4.11. At temperature higher than 200K, the data are quite off from fitted curves. We thus assume the temperature-dependence seen at higher temperatures is not an intrinsic property of Cs films, but more a property of how the films change, i.e., evaporate. Therefore, the temperature dependence at the higher temperatures is more a thickness driven by increased temperature dependence. From the core level spectra from Fig 4.2, we can see as the temperature gets high enough, the Cs spectra changes back to the low coverage spectra(The $5P_{3/2}$ peak is much broader than the bulk Cs and the calculated lifetime width is about 10 times wider than the bulk). We can also verify our assumption for the high temperature behavior by measuring the work function change with temperature. Fig 4.4 shows this measurement. We can see when the temperature is higher than 220K, the work function changes significantly compared to the work function below 200K. Also we know that the melting point for Cs is about 300K. So at low pressure, it would be reasonable to assume the Cs adsorption starts to melt or sublimate at T ~ 2/3 (300K) = 200K.

From the curve fitting, we get the value for G_{ph}^{surf} (0) = 28 meV, G_{ph}^{bulk} (0) = 23 meV. The ratio G_{ph}^{surf} (0) / G_{ph}^{bulk} (0) is about 1.22. The Debye temperature for the bulk θ_D is about 43K and 36K for the surface. The surface Debye temperature is about 1/6 smaller than the bulk. The coupling constant for the surface and bulk phonon modes is found to be as follows: $C_{surf} = 2.84 \cdot 10^{-3}$ eV^3 and $C_{bulk} = 2.12 \cdot 10^{-3}$ eV^3. Thus the ratio C_{surf} / C_{bulk} is 1.34. The results are smaller than the values obtained for Li in Ref[113]. We also studied the phonon broadening for Cs/Cu(100) system at 40 eV photon energy. (Fig 4.5) For this higher photon energy, the instrument resolution becomes worse by being 112 meV. The ratio of G_{ph}^{surf} (0) / G_{ph}^{bulk} (0) is 1.16 , similar to its 20eV phonon energy counterpart . The Debye temperature θ_D^{bulk} =30.5 K, θ_D^{surf} = 27.4 K. The surface Debye temperature is about 10% smaller than the bulk. The ratio of C_{surf} / C_{bulk} is 1.21 . It is even smaller than the 20 eV situation. Table 4.1 lists all the results from the two different photon energies.

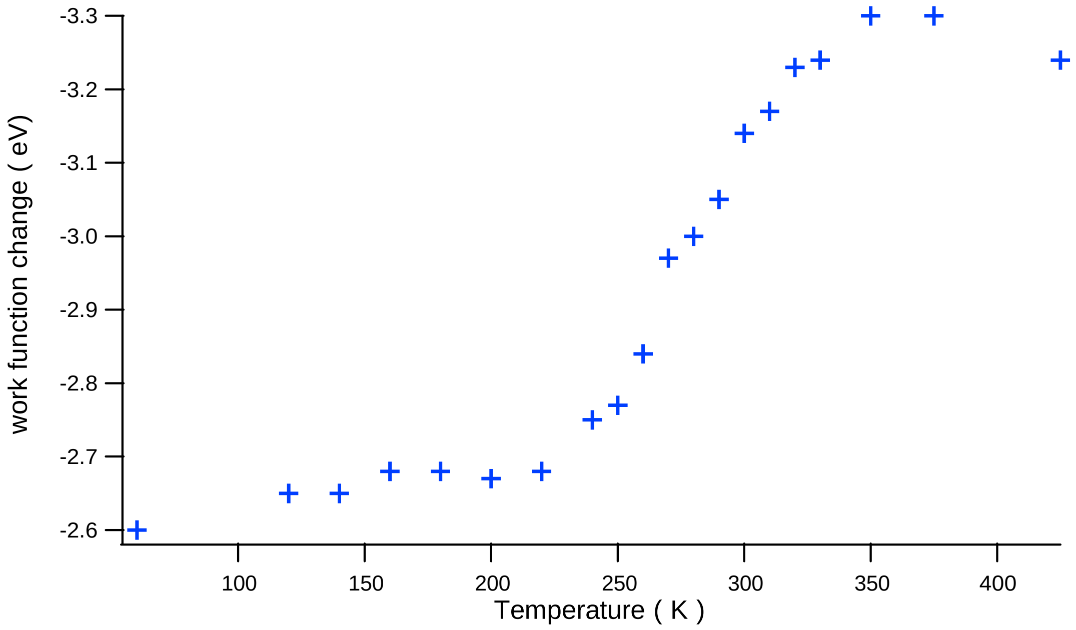

Fig 4.4 Change in work function vs. temperature for thick overlayer of Cs on Cu(100). Zero on this scale is the clean Cu (100) work function

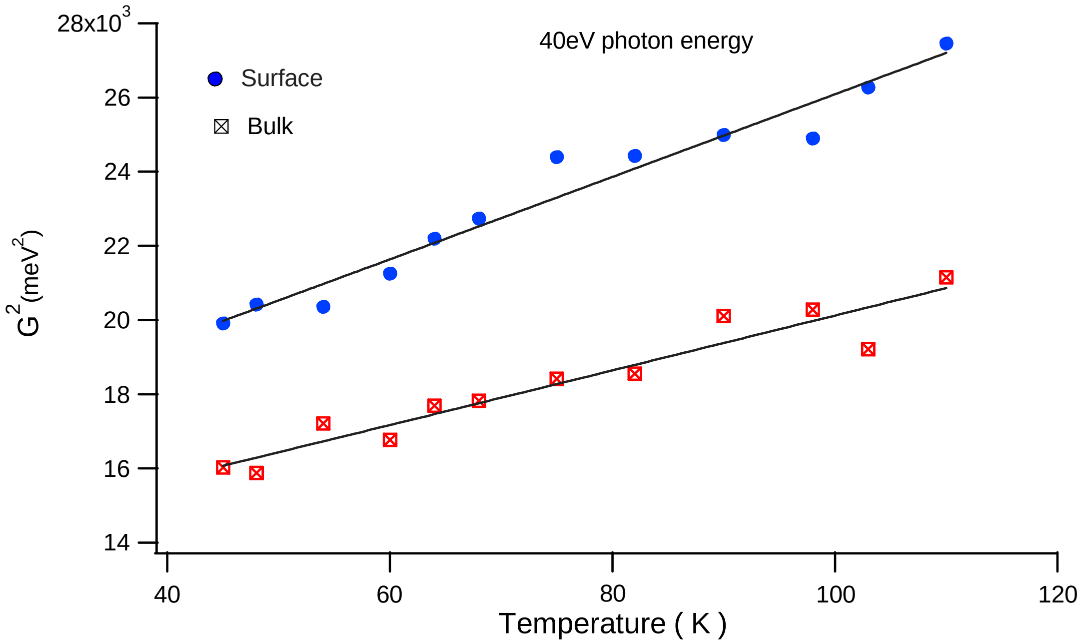

Fig 4.5 Square of Gaussian broadening vs. temperature for bulk and surface peaks fitting to Eq 4.11 for photon energies of 40eV.

Photon Energy (eV)	20	40
$G_{ph}^{surf}(0)(meV)$	28	34
$G_{ph}^{bulk}(0)(meV)$	23	29
$\theta_D^{surf}(K)$	36	27.4
$\theta_D^{Bulk}(K)$	43	30.5
$c_{surf}(10^{-3}eV^3)$	2.84	3.15
$c_{bulk}(10^{-3}eV^3)$	2.12	2.59
c_{surf}/c_{bulk}	1.34	1.22
$G_{ph}^{surf}(0)/G_{ph}^{bulk}(0)$	1.22	1.16
$\theta_D^{surf}/\theta_D^{bulk}$	0.84	0.90
G_{nst}(meV)	70	112

Table 4.1 The constants C and the zero temperature Gaussian broadening for the temperature dependent data at 20 and 40 eV photon energy for the Cs 5p3/2 core level peaks.

In conclusion, we studied the phonon broadening for Cs $5p_{3/2}$ core level peak on Cu(100) at different temperatures. We used the simplified Overhauser equation to fit our phonon broadening data and derived the Debye temperature and zero temperature phonon broadening. The Debye temperatures we got are close to the value measured by other experiment method. The ratio of coupling constant C_{surf} / C_{bulk} is smaller than Riffe's measurement for other alkali metals. Thus it is closer to Overhauser's theory.

4.2 Thermal shift for Cs $5p_{3/2}$ spectra

In this section, we are dealing with core level binding energy that is affected by valence electrons and vibration of lattice in a metal. For alkali metals, core electrons can be distinguished from the valence electrons. Although the core is highly localized and the wave function of a core electron is very weakly dependent on the valence band, the binding energies(or the energy levels) can be affected by the valence electrons quite a bit, causing a energy shift up to 10eV.[93, 96] One reason for the shift of the core level binding energy partly comes from changes in the Coulomb field around the core electron, and other is due to polarization effects. The polarization will happen when a core hole appears. When photon knocks off a core electron, valence electrons will be drawn in toward the positive core hole. Upon conduction electrons screen the suddenly created charge , the wave functions of each screening electron become modified to a degree that depends on their proximity to the core hole. The core level shift can reflect valence band changes caused by temperature because the lattice expansion due to higher temperature can affect the valence band and valence electrons send this changing information to the core. This kind of study has been reported in insulators and metals[93-95]. Riffe et al. investigated the thermal shifts for many alkali metals except Cs. [95] By using formalism given by Hedin, Lundqvish, J. Hozl and F.K. Schulte, they calculated the core level shifts caused by temperature. Their results fit experiments very well except for Li and Al (they used their calculation to compare with earlier experiment results for Al. [94]). They attribute the problem from Al and Li to deviations from free-electron character .

We measured the thermal shifts for Cs by using Riffe, J. Hozl and F.K. Schulte's methods. Basically the thermal shift of the core electron BE in a free-electron metal ΔE_{BE} comes from three contributions.[95] The first is due to the change with thermal expansion of the Fermi level, which is the reference level for measured core electron binding energies in a metal. It is written as from Ref [95]

$$\Delta E_F = \frac{-100.2}{r_s^2} + \frac{16.6}{r_s} + \frac{8.0\, r_s}{(r_s + 7.8)^2}\left[1 + \frac{r_s}{(r_s + 7.8)}\right] \frac{\Delta a}{a} \quad , \qquad (4.13)$$

Where r_s is the radius of a sphere containing one conduction electron, expressed in units of the Bohr radius a_0. The unit of energy is eV. To get this result, they considered the thermal expansion effect on the width of the occupied conduction band. They got the chemical potential formula from Ref [96, 97] and take the derivative of it with respect to r_s (The chemical potential is a value relative to the average internal potential of a free electron metal.) The lattice dimension change is replaced by the change $\Delta r_s / r_s$. The first term is negative and it proved to be the dominate term in the equation for most alkali metal. However for the Cs atom which has a large r_s, the value of Eq 4.13 is positive. Since this term is very small in Cs compared with other two reasons that affect the thermal shift, we'll not be concerned with it very much.

The second contribution to the thermal shift is caused by the decrease of conduction electron density. This decrease of the negative charge density around an ion will reduce the potential energy of the core electron. Riffe et al expressed this second contribution as

$$\Delta E_c = \frac{8.16}{{}_s} r1 - \frac{5^{\ 2}}{{}_s^{2}} l \frac{\Delta a}{a} \qquad (4.18)$$

To get this expression, they used Bardeen’s calculation for the undistorted potential in a cell, which is approximately equal to the potential of the ion in the center of the cell plus the potential of the electron cloud within the cell. [98]

$$V(\ ) = \frac{3e^2}{2a_0\,{}_s} - \frac{e^2\ {}^2}{2a^0\,{}_{s2}}, \qquad (4.14)$$

And the average potential inside the cell is

$$V_{av} = \frac{6eZ^{2/3}}{5a_0\,{}_s}\ , \qquad (4.16)$$

Eq 4.14 minus Eq 4.16, then take derivative with respect to ${}_s$,there will be Eq 4.15. They change the sign during the last step because thermal expansion always causes decrease of larger banding energy

The third and final contribution to the thermal shifts is the temperature dependent change of the relaxation energy. It can be expressed as (see Appendix of Ref [95]):

$$\Delta E^A_{rel} = \frac{\dfrac{10.61 \quad 1 + 1.222\ {}_s^{1/2}}{{}_s^{1/2} \quad 1 + 0.815\ {}_s^{1/2}\ {}^{3/2}}\Delta a}{a} \qquad (4.19)$$

The sum of the three contributions to the thermal shift from Eqs 4.13, 4.18, 4.19 give the net calculated shift ΔE_{BE} . Next we will compare our experiment result with this calculation. The ${}_s$ for Cs is 5.63 from Kittel’s book. The value of r^2 in Eq is set equal to

$({}^{2})$ for the relevant core electron and were taken from Ref [99]. We get the thermal expansion $\Delta a/a$ for Cs by interpolating the data from Ref [100]. Fig 4.6 shows the linear thermal expansion for Cs at different temperatures .

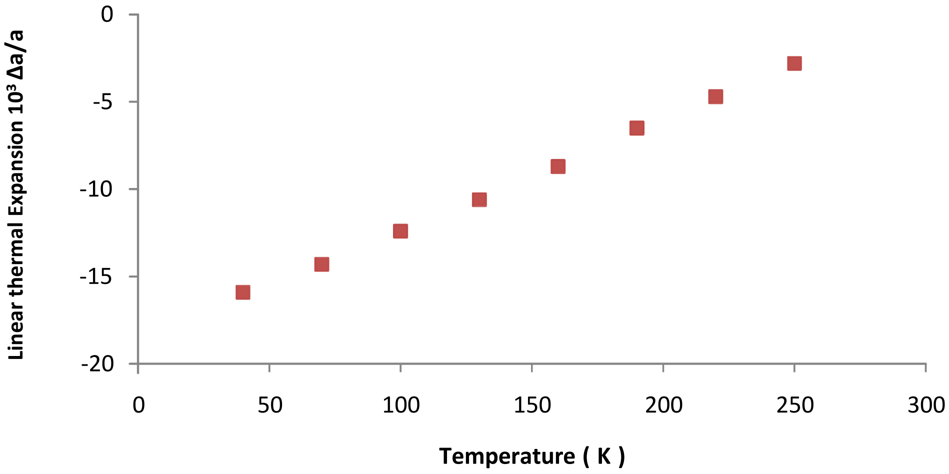

Fig 4.6 Linear thermal expansion for Cs

Fig 4.7 shows the thermal shifts for core level 5p3/2 electron peak at different temperatures for both experiment and calculation.

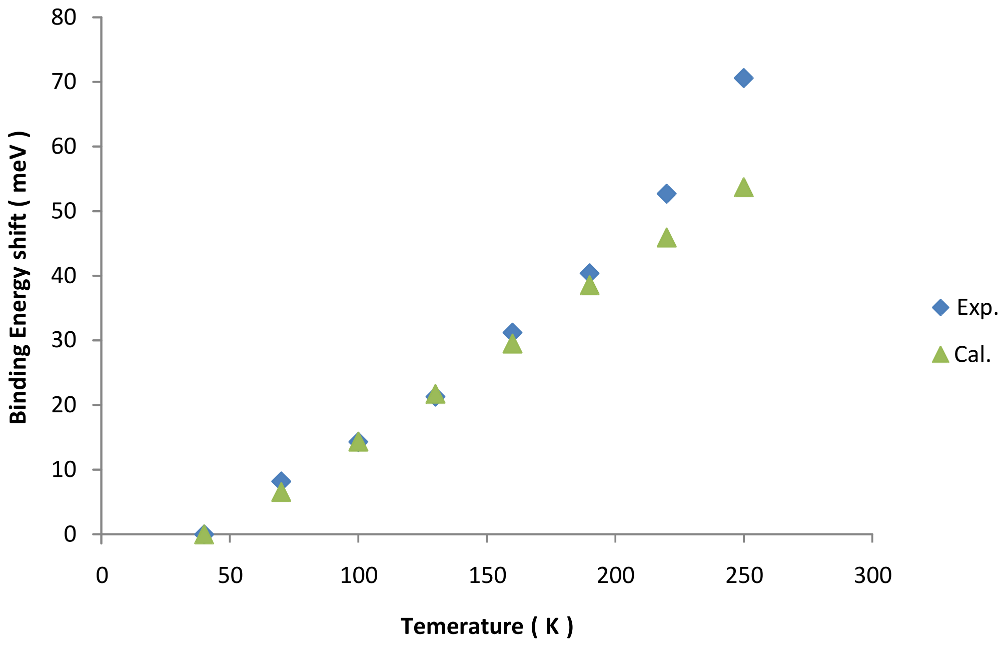

Fig 4.7 Cs $5p_{3/2}$ binding energy shift at different temperatures.

From the figure we can see that at temperature below 200K , the calculation fits the experiment very well with only a little off to the lower side. This successful fit proves the validation for the lattice expansion assumption. The result is better than Riffe's experiment for Na and K. But at temperature higher than 200 K, significant difference can be seen from the theory and experiment. A direct thought for this might be something wrong with the theoretical calculation. But if we think carefully, the answer would be the other way. We know the melting point for Cs is 300 K. So at temperature higher than 200 K , there might be sublime or evaporation for Cs in a UHV low pressure. If several monolayers of Cs is gone, the bulk peak might be changed a lot. So the higher temperature experiment data might not be the intrinsic character for Cs. We will verify this conclusion by other studies in the following sections. Table 4.2 shows the binding energy shift and the values for each of the three contributions to thermal shift at different temperatures.

Temperature(K)	**40**	**70**	**100**	**130**	**160**	**190**	**220**	**250**
10^3 Δa/a	0	1.6	3.5	5.3	7.3	9.4	11.2	13.1
ΔE_F (meV)	0	0.23	0.50	0.75	1.04	1.33	1.59	1.86
ΔE_C (meV)	0	0.62	1.36	2.06	2.83	3.65	4.35	5.08
ΔE^A_{rel}(meV)	0	5.75	12.5	18.9	25.6	33.5	40.0	46.8
ΔE_{BE}(meV) calc.)	0	6.6	14.4	21.7	29.5	38.5	45.9	53.7
ΔE_{BE}(meV)(expt.)	0	8.2	14.3	21.3	31.2	40.4	52.7	70.6

Table 4.2 Values of three contributions from lattice expansion theory for Cs 5p3/2 bulk binding energy thermal shifts and experiment values.

We can see that for Cs, the major contributions for the thermal core level binding energy shift are from decrease in conduction electron density and change of the relaxation energy. The effect caused by Fermi energy shift is very small. This result is consistent with studies on K, Rb and quite different from studies on Al, In[95].

In conclusion, we measured the Cs 5p $_{3/2}$ core level shifts for the bulk peak for Cs/Cu(100) at different temperatures. The shifts vs temperature relation fits the lattice expansion theory very well except at temperature higher than 220K. The high temperature off is due to the evaporation of Cs because Cs has a low melting point of 300K.

4.3 Coverage dependence of Cs/ Cu(100)

We also studied the coverage dependence of Cs / Cu(100) system. Fig 4.8 shows the general behavior of Cs as it is grown on Cu(100). The 5p binding energy in the first atomic layer is observed to be relatively constant and it decreases slowly at higher coverage. This is in significant difference from Cs/W(110) in Ref[115]， which shows rapid decrease in binding energy at higher coverage. So dipole repulsion might not be formed. There is no change in the second-layer binding energy with coverage, indicating there is no dipole moment associated with these atoms. The other notable feature is that the second-layer spectrum is much narrower than that of the first. When a thicker layer is deposited , the spectrum exhibits the two-peak structure similar to that observed in the study of bulk Cs. And one more important thing is that the first layer signal is not visible any more at higher coverage. This is quite different from the Cs/W(110) system where visible first layer signal could be caused by non-uniform overlayer or possible islands or clusters formation. For our Cs/Cu(100) system, the situation is much better , indicating a better quality film. The surface component of this thick layer has a slightly larger binding energy than that of the bulk , but is similar to the second layer. This indicates that the interaction of the Cs directly in contact with the Cu(100) substrate is on the similar level as any other Cs-Cs interaction.

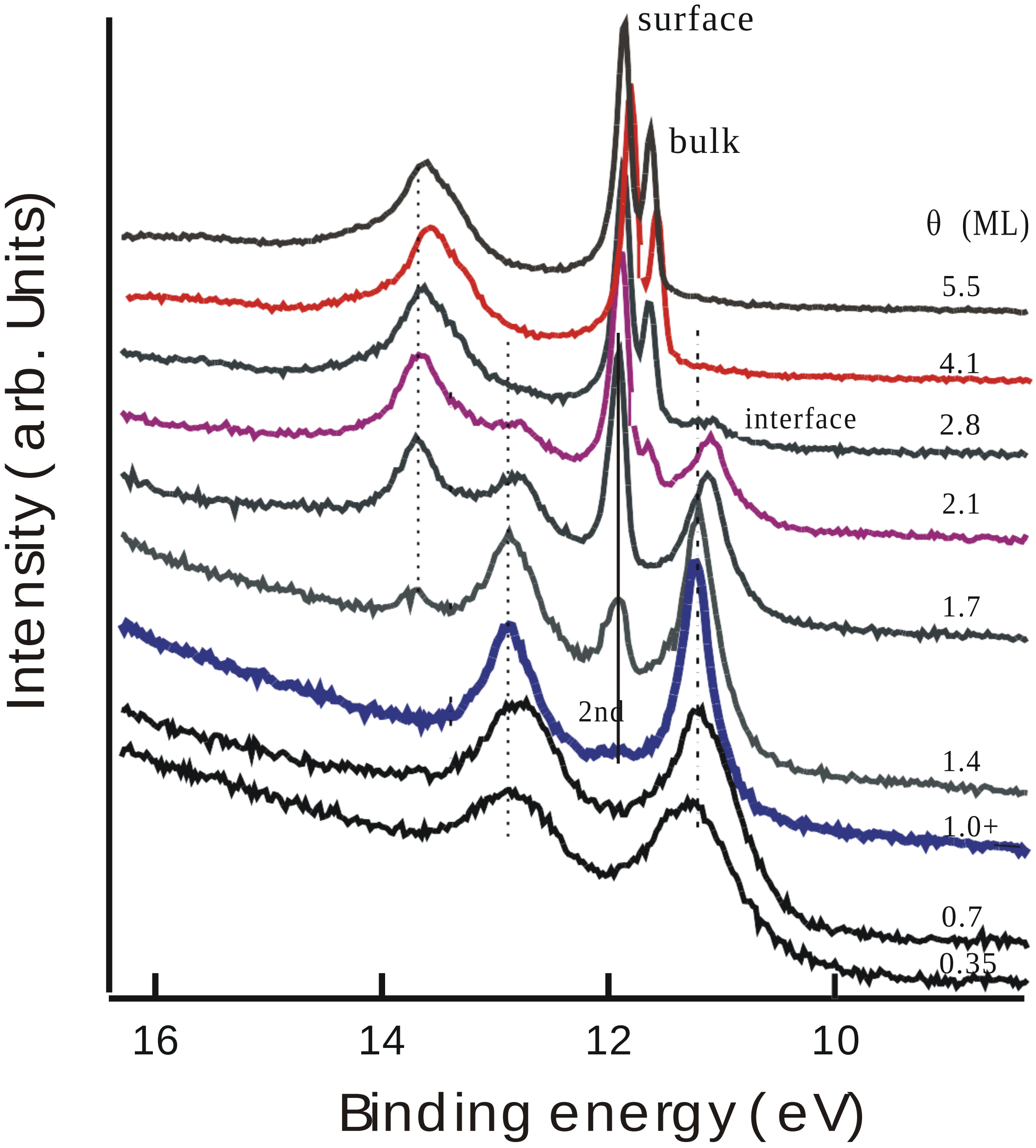

Fig 4.8 Photoemission study of Cs/Cu(100) film growth at different coverages with 30 eV photon energy.

We also studied the annealing behavior for thick Cs film on the Cu(100) substrate. The annealing temperature varies from 225K to 291K. From Fig 4.9 to Fig 4.11 we can see that when temperature increases , it is like having reducing adsorptions. It appears that the reduction to a simpler two layer system happens around 268K where the interface peak starts to appear. When the temperature gets to 291K, the film returns to sub-two monolayer situation. This also confirm the conclusion from the temperature dependence study in last section, that is when temperature gets to around 300K, the film just evaporate significantly.

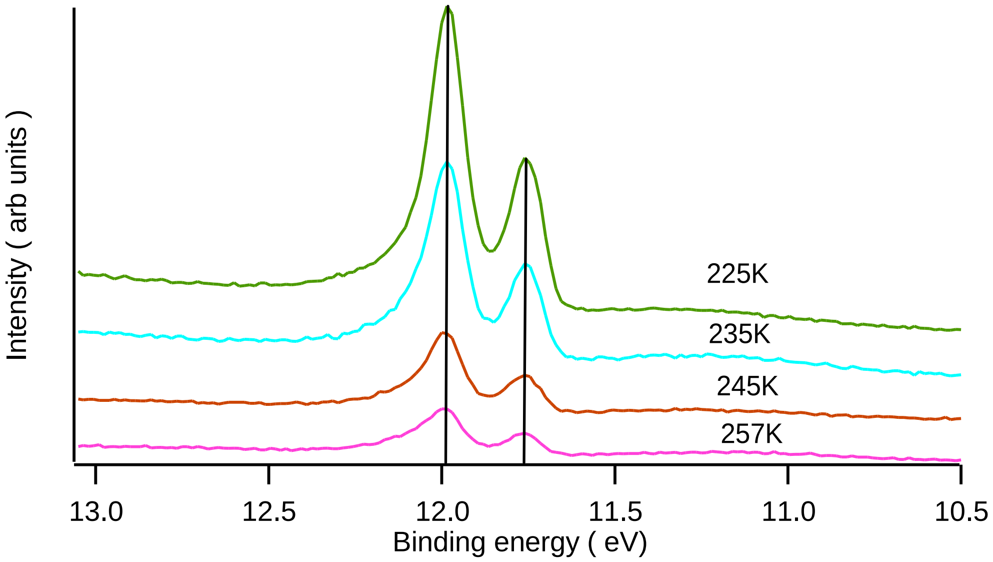

Fig 4.9 Thick Cs film (*:* = *8* ML) after heating to the temperature from 225 to 257K and cooling back to T *:::* 70 K.

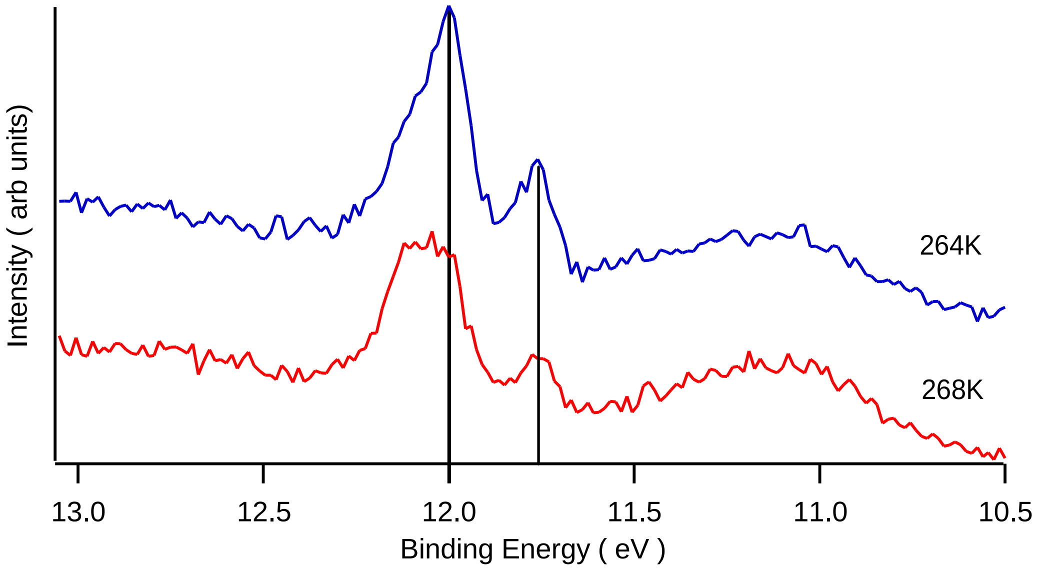

Fig 4.10 Thick Cs film (*:* = *8* ML) after heating to the temperature of 264 and 268K and cooling back to T *:::* 70 K.

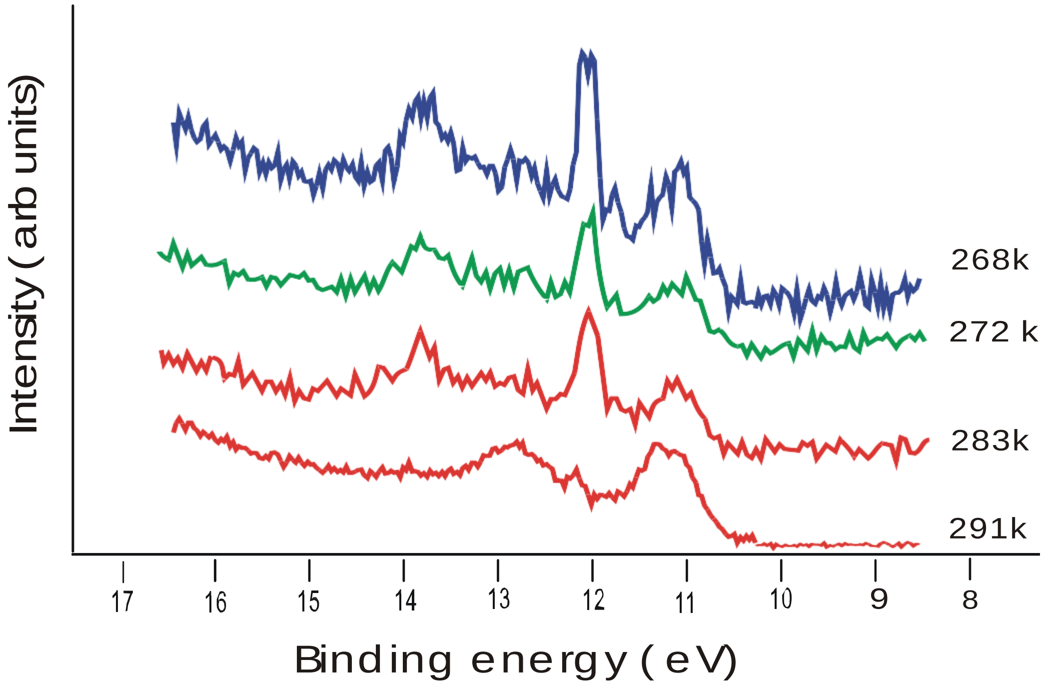

Fig 4.11 higher temperatures reproduce features of 2-1ML seen in the low coverage growth studies.

Bibliography

[1] .E. Felter, R. A. Barker, and P. J. Estrup, Phys. Rev. Lett. **38**, 1138 (1977).

[2] U. Gradmann and G. Waller, Surf. Sci. **116**, 539 (1982).

[3] M. Przybylski, I. Kaufmann, and U. Gradmann, Phys. Rev. B **40**, 8631 (1989).

[4] H. J. Elmers, J. Hauschild, and U. Gradmann, Phys. Rev. B **54**, 15 224 (1996).

[5] . D.M.Riffe, et. al., PRB 50, 14481(1994)

[6]. Jun-Hyung Cho, et.al. PRB 64, 115404(2001)

[7]. K.G. Purcell, J. Jupille, and D.A. King, Surf. Sci. **208**, 245(1989).

[8]. J. Gustaveson et al. PRL 91, 056102(2003)

[9]. A.M. Shikin et al., PRL 93, 146802(2004)

[10]. H.J.Elmers et al. PRL 73, 898(1994)

[11]. H.J. Elmers et al, PRB 59, 3688(1999)

[12], J.R. Ahn, PHYSICAL REVIEW B **75**, 033313 (2007)

[13] C. González, F. Flores, and J. Ortega, Phys. Rev. Lett. **96**, 136101(2006).

[14] H. W. Yeom, K. Horikoshi, H. M. Zhang, K. Ono, and R. I. G. Uhrberg, Phys. Rev. B **65**, 241307(2002).

[15] R. Meyer, C. Lemire, S. K. Shaikhutdinov, and H. Freund, Gold Bull. **37**, 72 (2004).

[16] M. Haruta, Catal. Today **36**, 153 (1997).

[17] C. R. Henry, Surf. Sci. Rep. **31**, 231 (1998).

[18] A. Sanchez, S. Abbet, U. Heiz, W.-D. Schneider, H. Hakkinen, R.S. Barnett, and U. Landmann, J. Phys. Chem. A **103**, 9573(1999).

[19] U. Heiz and W.-D. Schneider, J. Phys. D **33**, R85 (2000).

[20] M. Valden, X. Lai, and D. W. Goodman, Science **281**, 1647(1998).

[21] M. S. Chen and D. W. Goodman, Catal. Today **111**, 22 (2006).

[22] M. S. Chen and D. W. Goodman, Science **306**, 252 (2004).

[23] J. A. Rodriguez, G. Liu, T. Jirsak, J. Hebeck, Z. P. Chang, J. Dvorak, and A. Maiti, J. Am. Ceram. Soc. **124**, 5242 (2002).

[24] N. Lopez, J. K. Norskov, T. V. W. Janssens, A. Carlsson, A. Puig-Molina, B.S.Clausen, and J. D. Grunwaldt, J. Catal. **225**, 86 (2004).

[25] A. Varykhalov et al., PHYSICAL REVIEW B **75**, 205417 (2007)

[26] J. Bernasconi, T. Schneider (Eds.), Physics in One Dimension, Springer, Berlin, 1981.

[27] G. Gru¨ner, Density Waves in Solids, Addison-Wesley, Reading, MA 1994

[28] M. Grioni, I.Vobornik, F. Zwick, G. Margaritondo, J. Electr. Spectrosc. 100 (1999) 313.

[29] J.M. Luttinger, J. Math. Phys. 4 (1963) 1154.

[30] V. Meden, K. Scho¨nhammer, Phys. Rev. B 46 (1992) 15753.

[31] M.G. Zacher, E. Arrigoni, W. Hanke, J.R. Schrieffer, Phys. Rev. B 57 (1998) 6370.

[32] A. Luther, V.J. Emery, Phys. Rev. Lett. 33 (1974) 589.

[33] J.N. Crain, F.J. Himpsel, Appl. Phys. A, 82 (2006) 431.

[34] H. Ohnishi, Y. Kondo, K. Takayanagi, Nature 395 (1998) 780.

[35] V. Rodrigues, D. Ugarte, Phys. Rev. B 63 (2001) 073405.

[36] V. Rodrigues, J. Bettini, P.C. Silva, D. Ugarte, Phys. Rev. Lett. 91 (2003) 096801

[37] H.J. Elmers, J. Hauschild, H. Ho¨che, U. Gradmann, H. Bethge, D.Heuer, and U. Kohler, Phys. Rev. Lett. **73**, 898 (1994).

[38] T. Jung, R. Schlittler, J.K. Gimzewski, and F.J. Himpsel, Appl. Phys. A: Mater. Sci. Process. **A61**, 467 (1995).

[39] J. Shen, R. Skomski, M. Klaua, H. Jenniches, S. Sundar Manoharan, and J. Kirschner, Phys. Rev. B **56**, 2340 (1997).

[40] V. Repain, J.M. Berroir, S. Rousset, and J. Lecoeur, Surf. Sci. **447**, L152 (2000).

[41] P. Gambardella, M. Blanc, H. Brune, K. Kuhnke, and K. Kern, Phys. Rev. B **61**, 2254 (2000).

[42] P. Gambardella, M. Blanc, L. Bu¨rgi, K. Kuhnke, and K. Kern,Surf. Sci. **449**, 93 (2000).

[43] J.-L. Lin, D.Y. Petrovykh, A. Kirakosian, H. Rauscher, and F.J. Himpsel, Appl. Phys. Lett. **78**, 829 (2001).

[44] Himsel 1994 Cu on W

[45] R. P. Erickson and D. L. Mills, Phys. Rev. B **43**, 11 527 (1991).

[46] U. Gradmann, J. Magn. Magn. Mater. **54-57**, 733 (1986).

[47] E. Ising, Z. Phys. **31**, 253 (1925).

[48] E. Lieb and D. Mattis, Phys. Rev. **125**, 164 (1962).

[49] J. E. Hirsch, Phys. Rev. B **56**, 11022 (1997)

[50] S. Liang and H. Pang, Europhys. Lett. **32**, 173 (1995).

[51] S. Daul and R. M. Noack, Phys. Rev. B **58**, 2635 (1998).

[52] S. Watanabe, M. Ichimura, T. Onogi, Y. A. Ono, T. Hashizume, and Y. Wada, Jpn. J. Appl. Phys., Part 2 **36**, L929 (1997).

[53] E. H. Lieb, Phys. Rev. Lett. **62**, 1201 _1989_; H. Tasaki, Phys. Rev. Lett. **69**, 1608 (1992)

[54] J. D. Jackson, Classical Electrodynamics, third edition.

[55] S. Ferrer, Y. Petroff, Surface Science 500 (2002) 605

[56] J. Hauschild, H. J. Elmers, and U. Gradmann, Phys. Rev. B **57**, R677 (1998).

[57] H. J. Elmers, J. Hauschild, H. Fritzsche, G. Liu, U. Gradmann, and U. Ko¨hler, Phys. Rev. Lett. **75**, 2031 (1995).

[58] Elmers, et al. PRB 59, 3688(1999)

[59] C. Jensen, K. Resho¨ft, and U. Ko¨hler, Appl. Phys. A: Mater. Sci. Process. **62**, 217 (1996).

[60] D. Spišák* and J. Hafner, Phys. Rev. B **70**, 014430 (2004)

[61] H.J. Himsel, Journal of Electron Spectroscopy and Related Phenomena 75 (1995) 187

[62] M. Pauno and E. Bauer. Appl. Phys. A. 44 (1987) 201.

[63] T Jung. Y.W. Mo and F.J. Himpcel. Phys. Rev. Let.. 74(1995) 1631.

[64] Johansson L I, Glans P-A and Balasubramanian T , Phys. Rev. B **58** 3621(1998)

[65] M. T. Kief and W. F. Egelhof, Jr., J. Vac. Sci. Technol. A **11**, 1661 (1993).

[66] A. Brodde, K. Dreps, J. Binder, Ch. Lunau, and H. Neddermeyer, Phys. Rev. B **47**, 6609 (1993).

[67] Yina Mo et al. PRL **94,** 155503 (2005)

[68] P. Gambardella et al. , Nature 416, 301(2002).

[69] D. Spišák and J. Hafner, Phys. Rev. B **65**, 235405 (2002).

[70] M. Komelj, C. Ederer, J. W. Davenport, and M. Fähnle, Phys. Rev. B **66**, 140407(R) (2002).

[71] C. Ederer, M. Komelj, and M. Fähnle, Phys. Rev. B **68**, 052402(2003).

[72]A. B. Shick, F. Máca, and P. M. Oppeneer, J. Magn. Magn. Mater. **290-291**, 257 (2005).

[73] Hideki Fujisawa et al., Phys Rev. B **75**, 245423 (2007)

[74] P.H. Zhou et al, PRL **101,** 036807 (2008)

[75] *The Many-Body Problem*, edited by D. C. Mattis ,World Scientific, Singapore, 1993.

[76] Cheng et al, PHYSICAL REVIEW B **77**, 024404 (2008)

[77] A. Varykhalov, O. Rader, and W. Gudat, PHYSICAL REVIEW B **72**, 241404(R) (2005)

[78] A. Varykhalov, O. Rader, and W. Gudat, PHYSICAL REVIEW B **72**, 115440 (2005).

[79] A. Varykhalov, C. Biswas, W. Gudat, and O. Rader, PHYSICAL REVIEW B **74**, 195420 (2006).

[80] Andrew Zangwill. Physics at Surfaces. Cambridge University Press, Cambridge, 1988.

[81] Quantum Mechanics, Zeng Jinyan, Press of Science, 1981

[82] C. N.Berglund, W.E.Spicer, Phys. Rev. A 136, 1030 and 1044(1964)

[83] W. F. Egelho®, Jr. Core-level binding-energy shifts at surfaces and in solids. Surf.

Sci. Rep., 6:253,415(1987).

[84] Hans Lüth, *Surfaces and Interfaces of Solid Materials* (Springer, New York, 1995)

[85] http://www.phys.au.dk/~philip/q1_05/surflec/node22.html

[86] S. Doniach and M. S¸unji¶c. Many-electron singularity in x-ray photoemission and x-ray line spectra from metals. J. Phys. C, 3:285, 1970.

[87] P. H. Citrin, G. K. Wertheim, and Y. Baer. Many-body processes in x-ray photoemission line shapes from Li, Na, Mg, and Al metals. Phys. Rev., B16 , 4256(1977).

[88] James A. R. Samson. Line Broadening in Photoelectron Spectroscopy. Rev. Sci. Inst.,40(9):1174, 1969.

[89].Y. Margoninski, Contemporary Physics, 27, 203 (1986)

[90].A. Zangwill, *Physics at Surfaces*, Cambridge University Press, 1988.

[91] OrientExpress. J. Laugier and Associates. http://www.ccp14.ac.uk/ccp/webmirrors/ lmgp-laugier-bochu

[92] David Lacina, "Crystal Preparation and Low Energy Electron Diffraction Studies of V(100)", Masters Thesis, University of Texas at Austin, 2004.

[93] P.H.Citrin et al, Phys. Rev. B 16, 4256(1977).

[94] J. A. Tagle et al., Phys. Rev. B 21, 4552 (1980).

[95] D. M. Riffe, et al, Phys. Rev. B, 45, 6216 (1992).

[96] J. Holzl et al, in *Solid surface physics*, edited by G. Holer, Springer Tracts in Modern Physics Vol. 85(Springer , Berlin, 1979)

[97] N. D. Lang, et al., Phys.Rev.B 3, 1215 (1971)

[98] J.Bardeen, Phys. Rev. 52, 688(1937).

[99] C. Lu, et al., At. Data 3, 1(1971).

[100] Rosemary A. MacDonald et al. , Phys. Rev. B 29, 6489 (1984).

[101] H. P. Bonzel, Surf. Sci. Rep. **8**, 43 (1988).

[102] Marina Pivetta, et al, PHYSICAL REVIEW B **71**, 165430 (2005)

[103] K. M. Hock, J. C. Barnard, R. E. Palmer, and H. Ishida, Phys. Rev. Lett. **71**, 641(1993)

[104] Andersen J N, Lundgren E, Nyholm R and Qvarford M , *Surf. Sci.* **289** 307(1993)

[106]L. Hedin and A. Rosengren, J. Phys. F **7**, 1339 (1977).

[107] B. Bergersen, T. McMullen, and J. P. Carbotte, Can. J. Phys. **49**,3155 (1971).

[108] C.-O. Almbladh and A. L. Morales, J. Phys. F **15**, 991 (1985).

[109] P. H. Citrin, G. K. Wertheim, and Y. Baer, Phys. Rev. B **16**, 4256(1977).

[110] D. M. Riffe, G. K. Wertheim, and P. H. Citrin, Phys. Rev. Lett.**67**, 116 (1991).

[111] E. Weschke and G. Kaindl, J. Electron Spectrosc. Relat. Phenom.**75**, 233 (1995).

[112] E. Weschke, A. Hohr, S. Vandre, C. Schußler-Langeheine, F.Bødker, and G. Kaindl, J. Electron Spectrosc. Relat. Phenom.**76**, 571 (1995)

[113] D.M. Riffe and G.K.Wertheim, Phys. Rev. B 61, 2302(2000)

[114] Kevin Koch, Doctoral Dissertation, University of Texas at Austin, 2001.

[115] G. K. Wertheim, D. M. Riffe, and P. H. Citrin. Phys. Rev. B49, 4834(1994).

[116] Lab manual in surface physics group, UT-Austin.

[117] www-xfel.spring8.or.jp/cband/e/Undulator.htm

[118] Alden M, Skriver H L and Johansson B 1993 *Phys. Rev. Lett.* **71** 2457

[119] Feibelman P J and Stumpf R 1994 *Phys. Rev.* B **50** 17480

[120]J. N. Andersen, J. Phys: Condensed Matter 13, 11267(2001)

[121] R. Smouluchowsky, Phys. Rev. **60**, 661 (1941)

[122]. D.M.Riffe, at. at, PRL 63, 1976(1989)

[123] G.K. Wertheim et al, Phys. Rev. B **38**, 7820 (1988)

[124] H.P.Steinruck, et.al., PRB 32, 5032(1985)

[125] D.M.Riffe, et. al., PRB 50, 14481(1994)

[126] J.F. van der Veen, D.E. Eastman, A.M. Bradshaw, and S. Holloway, Solid State Commun. **39**, 1301 (1981).

[127] Jun-Hyung Cho, et.al. PRB 64, 115404(2001)

[128] G. K. Wertheim et al, Phys. Rev. B **30**, 4343 (1984)

[129] K.G. Purcell, J. Jupille, and D.A. King, Surf. Sci. **208**, 245(1989).

[130] D. Chaveau, P. Roubin, C. Guillot, J. Lecante, G. Treglia, M.C. Desjonqueres, and D. Spanjaard, Solid State Commun. **52**, 635(1984).

[131] D.M. Riffe, et al, Phys. Rev. Lett, 65, 219(1990).

[132] I. Langmuir, Phys. Rev. **43**, 224 (1933).

[133]R. W. Gurney, Phys. Rev. **47**, 479 (1935).

VITA

Xubing Zhou was born in Taiyuan, China. He received the degree of Bachelor of Science and Master of Science both from Peking University. He came to the University of Texas at Austin in 2001 and joined the Erskine surface physics group in summer 2003. From July 2007 to August 2008, he worked at the Center for Advanced Microstructure and Devices in Louisiana on the Texas/CAMD 6m-TGM beamline.

Permanent Address: 1923 Willow Creek Dr #305, Austin, TX 78741

This manuscript was typed by the author